



CFD simulations of spoked wheel aerodynamics in cycling: Impact of computational parameters



F. Malizia ^{a,b,*}, H. Montazeri ^{a,b}, B. Blocken ^{a,b}

^a Department of Civil Engineering, KU Leuven, Kasteelpark Arenberg 40 – Bus 2447, 3001, Leuven, Belgium

^b Department of the Built Environment, Eindhoven University of Technology, P.O. Box 513, 5600, Eindhoven, the Netherlands

ARTICLE INFO

Keywords:

Cycling aerodynamics
Cycling spoked wheel
CFD analysis
Computational grid
Rotation modeling
Turbulence modeling

ABSTRACT

Spoked wheels are commonly used in cycling races and their aerodynamic performance is a critical factor in the overall cycling performance, as the wheels can be responsible for about 10% of the total cyclist-bicycle drag. Although several computational fluid dynamics (CFD) simulations have been carried out for wheel aerodynamics in the past decades, it is still not clear to which extent the outcome of such simulations is sensitive to the computational parameters set by the user. The present paper aims at defining a framework for CFD simulations of an isolated spoked wheel by a systematic sensitivity analysis focused on the computational grid, wheel rotation modeling and turbulence modeling. The results show: (i) a high sensitivity to the wheel surface grid, $y^+ (< 4)$ and far-field growth rate (≤ 1.15); (ii) the wheel rotational approaches with moving reference frame (MRF) and hybrid MRF-RW (RW = rotating wall approach) can provide a satisfactory agreement with wind tunnel data available in the literature (+9.7% and -2.1% deviations, respectively); (iii) $k-\omega$ SST, γ -SST or realizable $k-\epsilon$ are suitable as turbulence models. This work is intended to stimulate the accurate and reliable application of CFD for the assessment and optimization of wheel aerodynamics.

1. Introduction

In the 2018 Tour de France, 12 different manufacturers provided the wheels for the 22 participating racing teams (Radley, 2018). In addition, each manufacturer had several wheels in their catalogue. The wheel selection from this large variety of commercially available options should ideally be based on their performance in terms of aerodynamic drag, weight, inertia and stiffness (Kyle, 1995). Earlier research has shown that the drag of both wheels can be responsible for about 10% of the combined cyclist-bicycle aerodynamic drag (Greenwell et al., 1995). In addition, it is well-known that the overall aerodynamic drag provides by far the largest contribution (up to 90% or more) to the total resistance of a cyclist riding at racing speeds on flat terrain (Kyle and Burke, 1984). From this perspective, even small aerodynamic improvements in different types of equipment can be effective to enhance the performance of a cyclist. Therefore, the accurate and reliable assessment and optimization of the aerodynamic performance of cycling wheels is of large importance.

To the best of our knowledge, the first cycling wheels selected for their aerodynamic performance were the disc wheels used by Francesco Moser for his world hour record in 1984 (Dal Monte et al., 1987) and the

disc and spoked wheels used by different cycling teams in the 1984 Olympic games. For example, Kyle and Burke (1984) described the aerodynamic tests performed to design the USA bicycles for the 1984 Olympic games. These tests included wind tunnel experiments of different wheels, which were held static during the tests. They found that narrower tires, fewer spokes, aerodynamic rim and smaller wheel diameters produced less drag. In addition, two wheel coast-down tests were performed by Kyle and Burke (1984) to estimate the wheel rotational moment. In the first type of tests, the wheel was put in rotation while fixed on a stand, then the rotational drag was estimated by measuring the rotational velocity deceleration. In the second type of tests, Kyle and Burke (1984) let the wheel roll down from a ramp and they measured its deceleration after the end of the ramp: this deceleration was a function of the wheel drag, rotational moment and rolling resistance. However no detailed information was provided about the wheels and the tests done, therefore these results cannot be used in the present paper for validation purposes.

Research on the aerodynamic performance of cycling in general and of wheels in particular is usually performed by either wind tunnel (WT) tests or – more recently – by numerical simulations with computational fluid dynamics (CFD) (Blocken, 2014; Crouch et al., 2017). An overview

* Corresponding author.

E-mail address: fabio.malizia@kuleuven.be (F. Malizia).

of WT and CFD studies on wheel aerodynamics will be given in section 2. A comparison of previous WT studies shows large deviations between WT tests on the same type of wheels between the different authors. These can be attributed to the type of wind tunnel, the wind tunnel test section (area, open versus closed), the approach-flow turbulence intensity, the use of front versus rear wheels, the inclusion of wheel rotation or not, wheels in proximity to the ground or not, and to measurement errors. WT tests of wheels cannot be performed without some type of support whereas the supports can be left out in the CFD simulations.

Although previous CFD studies employed different computational settings, to the best of our knowledge, a systematic investigation on the impact of computational parameters on the simulation results has not yet been performed. These computational parameters include the computational grid, the approach used to model the wheel rotation and the turbulence model. This indicates the need for an extensive and systematic sensitivity analysis to support future CFD studies on wheel and cyclist aerodynamics.

This situation with very large discrepancies in results and settings between different WT tests and the differences that can occur due to the large number of parameters to be set for CFD simulations removes confidence in current testing and simulation methods. Therefore, this paper intends to define a first framework for CFD simulations of an isolated spoked wheel throughout a systematic evaluation of the impact of different computational parameters. These computational parameters are the grid resolution, the wheel rotation modeling approach and the turbulence modeling. The CFD simulations are performed based on the 3D Reynolds-averaged Navier-Stokes (RANS) equations. The evaluation is based on the wind tunnel tests by Tew and Sayers (1999). This work is intended to stimulate the accurate and reliable application of CFD for the assessment and optimization of wheel aerodynamics either for isolated wheels or combined with the rest of the bicycle and the cyclist.

This paper focuses only on a single isolated wheel. In the past, it has been standard practice in both research and practical engineering in cycling aerodynamics to develop and optimize some components, such as wheels, based on the testing of these isolated components both in wind tunnel experiments and CFD simulations (e.g. Crane and Morton, 2018; Gibertini et al., 2010; Godo et al., 2010; Oggiano et al., 2009; Underwood et al., 2015; Zdravkovich, 1992). Nevertheless it has also been acknowledged that for assessing the final cyclist performance the whole system of cyclist together with all bicycle components should be considered. Note that even in configurations where the flow interference between the wheel and the other components is much larger, such as in cars, it is common practice to test wheels and tires in isolation. This is particularly the case for studies focused on determining optimal computational parameters and settings (e.g. Axon et al., 1998; Croner et al., 2013; Diasinos et al., 2015; Hobeika and Sebben, 2018; McManus and Zhang, 2006). Therefore, as a first step, the focus of this paper on an isolated wheel seems justified.

Section 2 contains a review of the literature and the state of the art.

Table 1
Wind tunnel tests of cycling wheel aerodynamics.

Reference	Test section [m ²]	Speed [km/h]	Yaw []	Wheel tested ^b	Reported results ^c	Rotational moment measured
Kyle (1990, 1991, 1995, 2002)	0.61 × 0.91	24–73	0, 10	Sp; a-Sp; disc	D	Yes
Zdravkovich (1992)	1.20 × 0.91	–	0–25	p-Sp	C _D , C _S , C _N ^d	No
Sayers and Stanley (1994)	0.87 × 0.58 ^a	30–72	0	c-Sp	C _D ^d	No
Greenwell et al. (1995)	1.52 × 2.13	16–48	0–90	Sp; a-Sp; disc	C _D , C _S , C _N ^e	No
Tew and Sayers (1999)	0.87 × 0.58 ^a	30–55	0–30	Sp; a-Sp; disc	C _D , C _S ^e	No
Jermy et al. (2008)	0.90 × 1.20	30–50	0–50	Sp; a-Sp; disc	D, S, P	Yes
Crane and Morton (2018)	1.00 × 1.00 ^a	32 - 59	0–12.6	Sp	C _D A, C _S A	No

^a Open test section. The dimensions refer to the wind tunnel jet.

^b Sp = spoked; a-Sp = aero-spoked wheels (tri-spoke, four-spoke and five-spoke wheels); p-Sp = spoked wheels with splitter plates; c-Sp = spoked wheels with cladding; disc = disc or lenticular wheels.

^c D = drag; S = side force; C_D = drag coefficient; C_S = side force coefficient; C_N = yawing moment coefficient; P = power; C_DA = drag area; C_SA = side force area.

^d Coefficients computed using frontal area $2dr$, where d is tire width and r the wheel radius including the tire.

^e Coefficients computed using lateral area, πr^2 , where r is the wheel radius including the tire.

The wind tunnel experiments of Tew and Sayers (1999) are introduced in Section 3 together with the description of the selected wheel for this study (Campagnolo Shamal). Section 4 presents the computational settings and parameters for the reference case. The sensitivity analysis is presented in Sections 5–7 where the impact of the computational grid (Section 5), the wheel rotation modeling (Section 6) and the turbulence modeling (Section 7) is reported. Finally, the paper concludes with discussion (Section 8) and conclusions (Section 9).

2. Literature review and state of the art

Table 1 provides an overview of WT studies on wheel aerodynamics specifying the WT test section, the speeds and yaw angles at which the tests were performed, the type of wheels tested, the way in which the results were reported and whether or not the rotational moment was measured. In the majority of these studies, the aerodynamic performance of different commercially available wheels (Crane and Morton, 2018; Greenwell et al., 1995; Jermy et al., 2008; Kyle, 1990, 1991; 1995, 2002; Tew and Sayers, 1999) was evaluated. The measurements were performed on isolated wheels for all studies listed in **Table 1**.

The first systematic WT analysis of wheel aerodynamics was performed by Kyle (1990, 1991, 1995, 2002). In these studies, about 30 wheels were considered and their total aerodynamic drag was provided as the sum of the translational aerodynamic drag and the equivalent aerodynamic drag computed from the rotational moment measurements. Noted that the aerodynamic rotational moment originates from the wheel rotation. The directions of the drag, D, and rotational moment, M, together with the directions of the wind velocity, U, and wheel rotational velocity, ω, are provided in Fig. 1. Jermy et al. (2008) mentioned the high impact of the rotational moment, to be up to 53% of the aerodynamic power required to move the wheel. Therefore, both drag and rotational moment need to be jointly considered to correctly assess the wheel performance. Nevertheless, in most wind tunnel tests the rotational moment is not evaluated while the measurements are limited to drag and

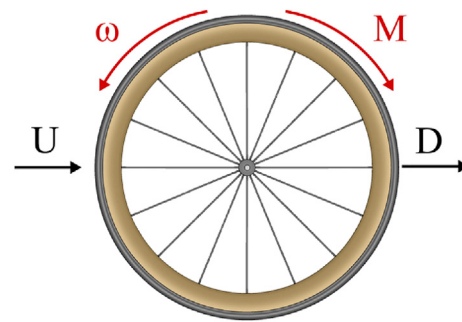


Fig. 1. Direction of drag force (D), rotational moment (M), wind velocity (U) relative to wheel translation and wheel rotational velocity (ω).

side force ([Table 1](#)).

However, even drag force results alone measured for the same type of wheel showed discrepancies between different studies. For example, [Greenwell et al. \(1995\)](#) and [Tew and Sayers \(1999\)](#) tested 7 and 6 wheels respectively, among which two wheels were the same: the Campagnolo Shamal spoked wheel and the Specialized tri-spoke wheel. [Tew and Sayers \(1999\)](#) measured a much lower drag value at 0° yaw angle compared to [Greenwell et al. \(1995\)](#): 37% and 16% lower for the spoked and tri-spoke wheel respectively. These high deviations were likely caused by the different wind tunnel configuration and setup: [Greenwell et al. \(1995\)](#) tested rear wheels, attached to a cut rear-section of a bicycle frame, in a closed test-section wind tunnel with the wheel in proximity to the ground, while [Tew and Sayers \(1999\)](#) tested front wheels in an open test-section wind tunnel without a ground plate and with only one strut supporting the wheel. Nevertheless, both studies found that aerodynamically-designed wheels experienced similar or a smaller axial resistance when the yaw angle was increased ([Greenwell et al., 1995](#); [Tew and Sayers, 1999](#)), while the opposite trend was found for the other wheels. The reduction in axial resistance, i.e. the aerodynamic resistance aligned with the wheel, is caused by the interaction with the lateral force generated by the aerodynamically-shaped rims in crosswind conditions. Moreover, it was found that the approach-flow wind speed (between 16 km/h and 48 km/h) had a small effect on the wheel aerodynamics, causing a negligible Reynolds number dependency ([Greenwell et al., 1995](#)).

Next to these comparisons, other wind tunnel studies aimed at reducing the wheel resistance by means of splitter plates ([Zdravkovich, 1992](#)) or cladding ([Sayers and Stanley, 1994](#)). The first consisted of thin plates of different length added internally to the wheel near the rim, while the second were cardboard disks placed over the spokes on both wheel sides. Including splitter plates to cycling wheels reduced the drag coefficient up to 4% ([Zdravkovich, 1992](#)). Fully cladded wheels were as good as disc wheels at speeds of 15 m/s and 20 m/s, whereas partially cladded wheels had more than 40% higher drag compared to commercial disc wheels ([Sayers and Stanley, 1994](#)). Furthermore, [Zdravkovich \(1992\)](#) noted a high drag sensitivity to the wheel alignment with the incoming flow: 10% difference in drag coefficient was found between 0° and 2° yaw angle.

The complexity of wheel aerodynamics was also highlighted by the work of [Crane and Morton \(2018\)](#), where a high sensitivity was observed of the drag to the ratio between tire-width to rim-width, after testing several wheel-tire combinations in a wind tunnel. From the linear regression provided by [Crane and Morton \(2018\)](#), we deduce that a 10%

wider tire will increase the drag of the isolated wheel by about 3%.

The discrepancy found in the aerodynamic drag between different wind tunnel results on the same wheel ([Greenwell et al., 1995](#); [Tew and Sayers, 1999](#)) was also reported by [Godo et al. \(2009, 2010, 2011\)](#). They performed CFD simulations of six different wheels, ranging from spoked wheels to tri-spoke and disc wheels, and compared their results with wind tunnel results available in literature or provided by wheel manufacturers. Note that these manufacturer data have not been substantiated and should be treated with caution. For example, the measured drag coefficient for the Zipp 404 spoked wheel at 0° yaw angle ranged between 0.017 and 0.051 in different experiments, while the computed drag coefficient was about 0.029. At yaw angles larger than 0°, the computed drag coefficient was 29% to 45% lower than the WT results. It is worth to note that only one set of WT data from a wheel manufacturer was available at different yaw angles. This highlights the difficulty in reproducing results not only between different WT tests, but also between WT tests and CFD simulations.

[Table 2](#) provides an overview of CFD studies on wheel aerodynamics. Although these studies employed different computational settings, to the best of our knowledge, a systematic investigation on the impact of computational parameters on the simulations results has not yet been performed. These computational parameters include the size of the computational domain, the computational grid, the approach used to model the wheel rotation and the turbulence model. The computational parameters used in previous CFD studies are briefly discussed below.

The domain size by [Karabelas and Markatos \(2012\)](#) was the only to agree with the CFD best practice guidelines for outdoor flows in the urban environment about the domain extents ([Blocken, 2015](#); [Franke et al., 2007, 2010](#); [Tominaga et al., 2008](#)) and automotive external aerodynamics ([Lanfrat, 2005](#)), while the other CFD studies had smaller computational domains. Note however that due to the slenderness of the wheel, narrower domains might be sufficient, although further investigations are required to confirm this. The total cell count of the computational grid also varied significantly in these different studies: from less than 1 M cells ([Karabelas and Markatos, 2012](#)) to about 5 M cells ([Knupe and Farmer, 2009](#); [Pogni and Petrone, 2016](#)) and between 4 M and 16 M cells ([Godo et al., 2009, 2010, 2011](#)).

Different approaches were also used to model the wheel rotation. [Knupe and Farmer \(2009\)](#) and [Pogni and Petrone \(2016\)](#) modeled the wheel rotation using a moving reference frame (MRF) approach applied to a volume surrounding the entire wheel, while [Godo et al. \(2009, 2010, 2011\)](#) applied the MRF approach only on a volume surrounding the inner wheel (hub, spokes and inner rim) and a rotating wall boundary

Table 2
CFD simulations of cycling wheel aerodynamics.

Reference	Wheel ^a	Domain (W x H x L) ^c	Grid ^e	Turbulence modeling ^f	Rotational modeling ^g	Comparison with WT tests
Knupe and Farmer (2009)	Sp; a-Sp; disc	1.4 × 1.2 × 5.0 m ³ (2.0Ø × 1.7Ø × 7.1Ø)	1 M–6 M	Std k-ε	MRF	No
Godo et al. (2009, 2010)	Sp; a-Sp; disc	0.8 × 1.1 × 2.8 m ³ (1.2Ø × 1.5Ø × 4Ø)	3.8 M–16 M	SA-DES	MRF-RW	Yes
Godo et al. (2011)	Sp; a-Sp; disc ^b	Semi-ellipsoid ^d	6 M–10 M	SA-DDES	MRF-RW	Yes
Karabelas and Markatos (2012)	Sp	4.2 × 4.2 × 14.0 m ³ (6Ø × 6Ø × 20Ø)	250 k – 522 k	URANS	SM	Yes ^h
Pogni and Petrone (2016)	Sp	1.5 × 1.2 × 2.0 m ³ (2.1Ø × 1.7Ø × 2.9Ø)	Up to 5 M	Std k-ε	MRF	No

^a Sp = spoked; a-Sp = aero-spoked wheels (tri-spoke, four-spoke and five-spoke wheels); disc = disc or lenticular wheels.

^b Bicycle front-half included in the simulations.

^c Wheel diameter, Ø, assumed to be 0.7 m.

^d No size provided.

^e ‘k’ is used for thousands (10³) and ‘M’ for millions (10⁶).

^f Std k-ε = standard k-ε; SA = Spalart Allmaras; DES = detached eddy simulation; DDES = delayed detached eddy simulation; URANS = unsteady RANS with Re-Normalization Group k-ε turbulence model.

^g RW = rotating wall; MRF = moving reference frame; MRF-RW = hybrid MRF and RW; SM = sliding mesh.

^h Only static wheel.

condition (RW) to the outer wheel (outer rim and tire). The latter approach is referred to in the present paper as hybrid MRF-RW. Lastly, Karabelas and Markatos (2012) modeled the wheel rotation by rotating the wheel during the simulation using a sliding mesh approach (SM). The volume where the MRF or SM approaches were applied varied from an arbitrary shape (Knupe and Farmer, 2009) over a cylindrical (Pogni and Petrone, 2016) to a double cone shape (Godo et al., 2009, 2010, 2011).

Table 2 also indicates that in the vast majority of CFD studies, the 3D steady Reynolds-averaged Navier-Stokes (RANS) were employed (Godo et al., 2009, 2010, 2011; Knupe and Farmer, 2009; Pogni and Petrone, 2016) while in few cases unsteady RANS (Karabelas and Markatos, 2012) and Delayed Detached Eddy Simulations (DDES) (Godo et al., 2009, 2010, 2011) were also employed. The larger use of RANS in cycling and cycling wheel aerodynamics is in line with the choice in many other topics of wind engineering and industrial aerodynamics (Blocken, 2014, 2018). The turbulence models used for the RANS equations ranged from the standard k- ϵ model (Knupe and Farmer, 2009; Pogni and Petrone, 2016) to the Spalart-Allmaras model (Godo et al., 2009, 2010, 2011). These equations were solved using a low-Reynolds number modeling approach (Pogni and Petrone, 2016) or by wall functions (Karabelas and Markatos, 2012). Accordingly, the average y^+ value was reported to be about 1 by Pogni and Petrone (2016) and between 30 and 70 by Karabelas and Markatos (2012), while Godo et al. (2009, 2010, 2011) only provided the dimensional height of the wall-adjacent cell: 0.25 mm.

3. Wind tunnel measurements

In this study, the wind tunnel measurements by Tew and Sayers (1999) are used for CFD validation. In these experiments, the aerodynamic forces were measured for six different wheels (Fig. 2): a conventional 36-spoke wheel (Fig. 2a), two wheels with aerodynamically-shaped rims and 16 (Fig. 2b, see also Fig. 3a) and 12 spokes (Fig. 2c) respectively, a four-spoke wheel (Fig. 2d), a tri-spoke wheel (Fig. 2e) and a disc wheel (Fig. 2f). The reported measurement accuracy for the drag force and side force was 0.02 N and 0.05 N, respectively. The wheel rotational moment was not measured, although the wheel was rotating according to the approach-flow wind speed.

The measurements were performed in an open test-section wind tunnel with uniform approach-flow conditions and turbulence intensity of 0.4%. The wind tunnel jet had a cross-section of 870 mm × 580 mm. The open test-section had a length of 1600 mm, with a 2.6% maximum streamwise velocity variation along the test-section. The isolated wheels were supported by a vertical strut connected to one hub-end (Fig. 3b). The wheel rotation was achieved using a DC motor that was in contact with the outer tire. The drag of the wheel support system was initially measured while the wheel was not present, and later subtracted from the wheel drag measurements. Tew and Sayers (1999) did not provide any additional information about other WT data corrections.

In the present study, the Campagnolo Shamal wheel (Fig. 3a) was selected from the wheels tested by Tew and Sayers (1999), since detailed information about the rim and hub profiles of this wheel could be retrieved from the 1996 Campagnolo catalogue (Campagnolo, 1996). Moreover, Tew and Sayers (1999) specified that the tire used in the experiment was a 20c tire, thus a tire with a nominal width of 20 mm.

The WT measurements were performed for different approach-flow wind speeds (U), representing the cycling speed, wheel rotational velocities (ω), and yaw angles. In the present study, the case with 0° yaw angle is considered, where $U = 13.41$ m/s (48 km/h or 30 mph) and $\omega = 38.32$ rad/s (366 rpm). For this case, the drag coefficient (C_D) was extrapolated from the graphs in (Tew and Sayers, 1999) to be 0.0236 ± 0.0005 . The latter number, 0.0005, is derived from the drag force balance accuracy. In addition to the drag coefficient, in the present study we include the rotational moment coefficient (C_M) due to its impact on the total cyclist performance (Jermy et al., 2008; Kyle, 1995). These two coefficients are defined in Eq. (1):

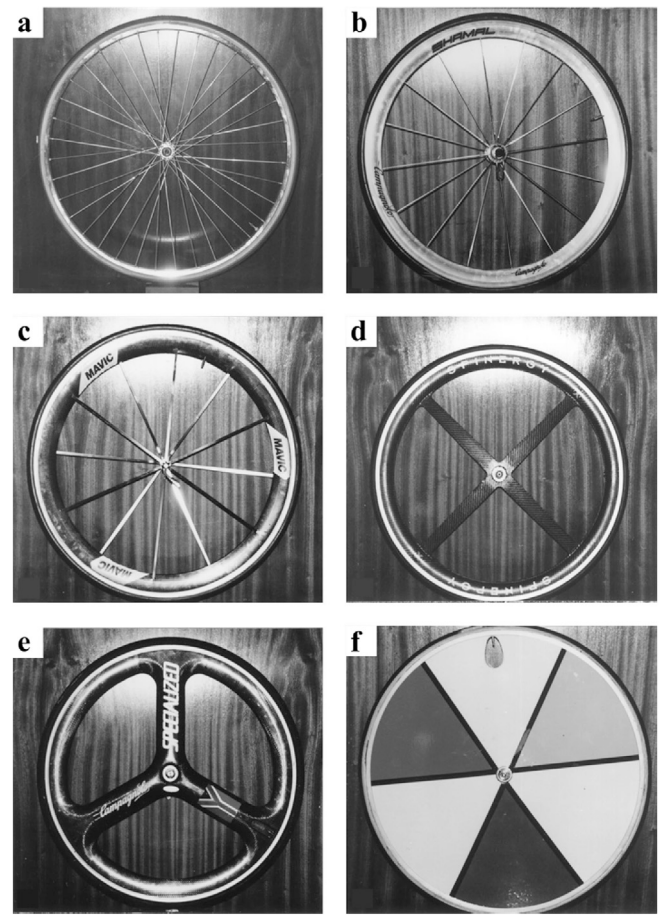


Fig. 2. Wheels tested by Tew and Sayers (1999): (a) Standard 36 spoked; (b) Campagnolo Shamal; (c) Mavic Cosmic; (d) Spinergy; (e) Specialized tri-spoke; (f) disc wheel. The Campagnolo Shamal wheel (2b) is the wheel under analysis in the present paper. Figure adapted from (Tew and Sayers, 1999). Reproduced with permission from Elsevier.

$$C_D = \frac{D}{0.5\rho AU^2}; \quad C_M = \frac{M}{0.5\rho ArU^2} \quad (1)$$

where ρ is the air density, D the drag force, M the rotational moment, U the wind velocity component parallel to the wheel (in m/s) and A the side area of the wheel with radius r (i.e. $A = \pi r^2$). The use of the side area as reference area rather than the frontal area is in line with the recommendation by Greenwell et al. (1995). Note that the use of the frontal area as reference area could be misleading since wheels with larger tire may have a higher drag but a lower drag coefficient than wheels with narrower tires (Greenwell et al., 1995).

4. CFD simulations: reference case

A reference case is defined as a starting point for the sensitivity analyses. This section presents the computational geometry and grid, boundary conditions and solver settings for the reference case. This reference case is systematically modified in terms of the following computational parameters: grid resolution (Section 5), rotational modeling (Section 6) and turbulence modeling (Section 7). A proper setting of each computational parameter is selected after each corresponding sensitivity analysis and it is used for the subsequent analyses. Lastly, the results are compared with the WT results of Tew and Sayers (1999).

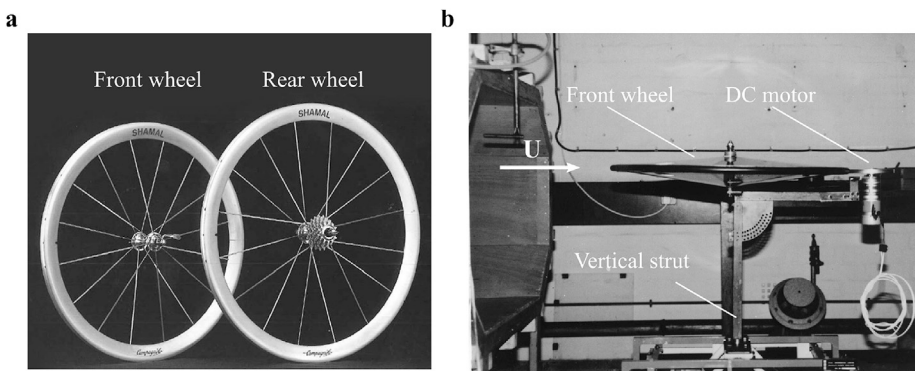


Fig. 3. (a) Front and rear Campagnolo Shamal wheels (adapted from www.campagnolo.com); (b) Tew and Sayers wind tunnel setup (adapted from [Tew and Sayers, 1999](#)). Reproduced with permissions from Campagnolo and Elsevier.

4.1. Computational geometry

The geometry of the Campagnolo Shamal spoked wheel is generated using the software ANSYS/SpaceClaim 18.2 ([ANSYS SpaceClaim, 2017](#)). The wheel is composed of four elements: rim (Fig. 4a), tire (Fig. 4c), hub (Fig. 4d) and spokes. The rim and hub profiles are obtained from the [Campagnolo 1996 catalogue](#) ([Campagnolo, 1996](#)): the rim has a 19 mm width and a 61 mm depth (combining rim and tire), while the hub has a length of 100 mm. The tire is modeled with a shape available in the literature ([Godo et al., 2009](#)) that has a 20.5 mm width, comparable with the 20c tire used by Tew and Sayers in their experiment ([Tew and Sayers, 1999](#)). Note that the actual geometry of the spokes, which is mentioned in [Tew and Sayers \(1999\)](#) as being thin elliptical – without further specifications – has been approximated in this paper as a rectangle with a 3 mm × 1 mm depth and width, respectively. The validity of this assumption is ascertained by additional CFD simulations in [Appendix A](#). The complete wheel is shown in Fig. 4b.

4.2. Computational domain and grid

The computational domain is shown in Fig. 5. Its dimensions are chosen based on CFD best practice guidelines for outdoor flows in the urban environment ([Blocken, 2015](#); [Franke et al., 2007, 2010](#); [Tominaga et al., 2008](#)) and automotive external aerodynamics ([Lanfrit, 2005](#)). The distances of the wheel geometry to the lateral, top and bottom planes of the domain are 5ϕ , where ϕ (= 700 mm) is the wheel diameter. The upstream and downstream length of the domain are 5ϕ and 10ϕ , respectively (Fig. 5a and c). Note that the presence of the ground is neglected, in line with the experiments by [Tew and Sayers \(1999\)](#) where the ground was also absent (Fig. 3b).

In the reference case, the wheel rotation is modeled using the moving reference frame approach (MRF). To do so, an interface separates the fluid domain in two distinct zones, the inner zone including the entire wheel, and the outer zone that includes the rest of the domain. This inner fluid zone is used to apply the MRF approach to model the wheel rotation. For the reference case, the MRF volume has a cylindrical shape positioned around the rotational axis of the wheel (Fig. 5b and d). The distance between the MRF volume faces and the wheel-ends is 25 mm. The impact of this distance and of the MRF volume shape will be systematically analyzed in Sections 6.1 and 6.2, respectively, while the impact of the rotational modeling approach will be investigated in Section 6.3.

The computational grid is generated in two steps. First, the Gambit software is used to create the wheel surface grid, as shown in Fig. 6. Next, ANSYS/Fluent Meshing is used to refine/coarsen the surface grid and to create the volume grid. Quad-cells are chosen for discretizing the spoke surfaces to reduce the number of cells on the spokes (Fig. 6c). The remaining wheel surface is spatially discretized using triangular cells. For the reference case, the cell edge size along the spoke width and depth is equal to 0.1 mm, resulting in about 758,000 surface cells for the entire surface of the wheel (including all components). A detailed sensitivity analysis for the impact of the number of surface cells will be provided in Section 5.1.

The fluid volume in the immediate vicinity of the wheel surface is spatially discretized with a series of prism layers, composed of wedge and hexahedral cells, while tetrahedral cells are used further away from the surface, i.e. in the far-field domain (Fig. 7) and pyramid cells are used in the transition zone between hexahedral and tetrahedral cells. The height of the wall-adjacent cells in the prism layer is 0.025 mm, which provides an average and maximum y^+ of about 0.9 and 2.6 respectively, for an

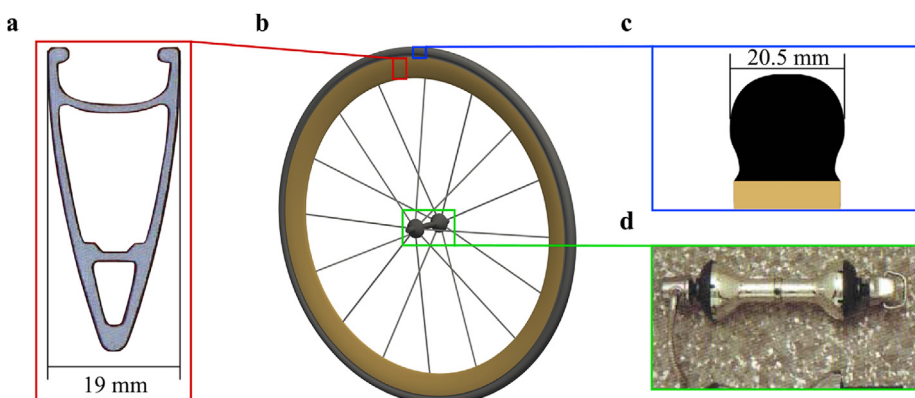


Fig. 4. Campagnolo Shamal spoked wheel: (a) rim profile (adapted from [Campagnolo, 1996](#)); (b) wheel computational geometry; (c) tire profile; (d) hub ([Campagnolo, 1996](#)). Fig. 4a and d reproduced with permission from Campagnolo.

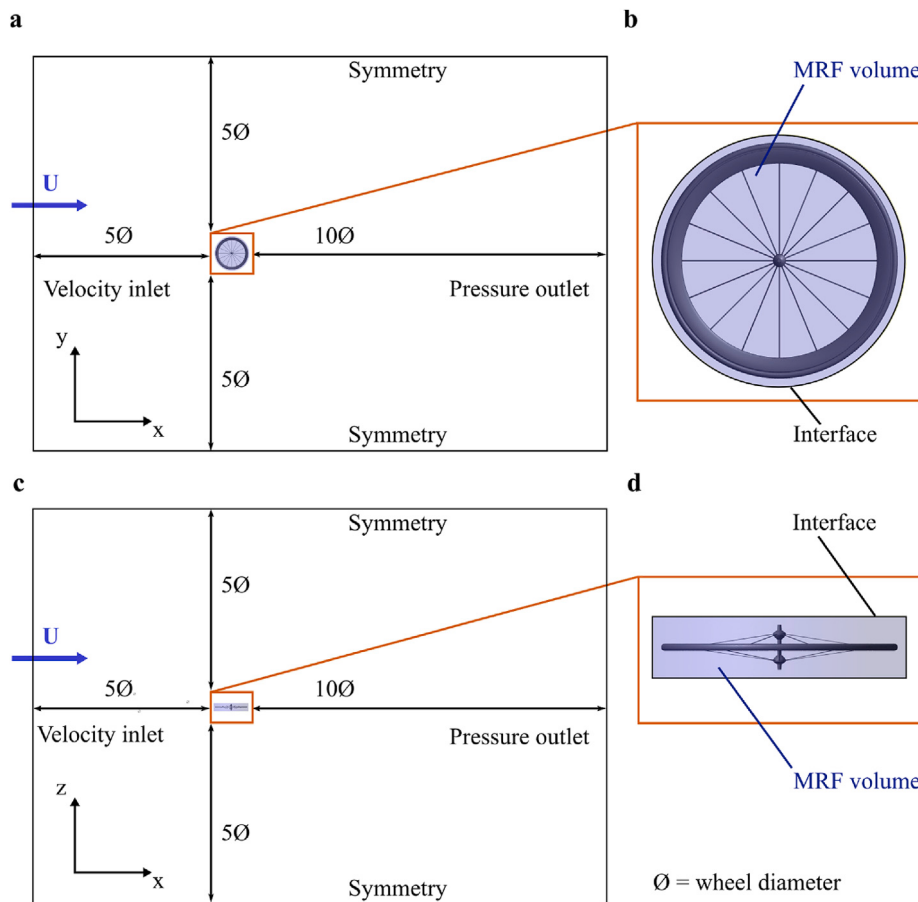


Fig. 5. (a) Side and (c) top view of the computational domain, including boundary conditions and main dimensions. The interfaces used to model the wheel rotation and to yaw the wheel are shown in (b) side and (d) top view.

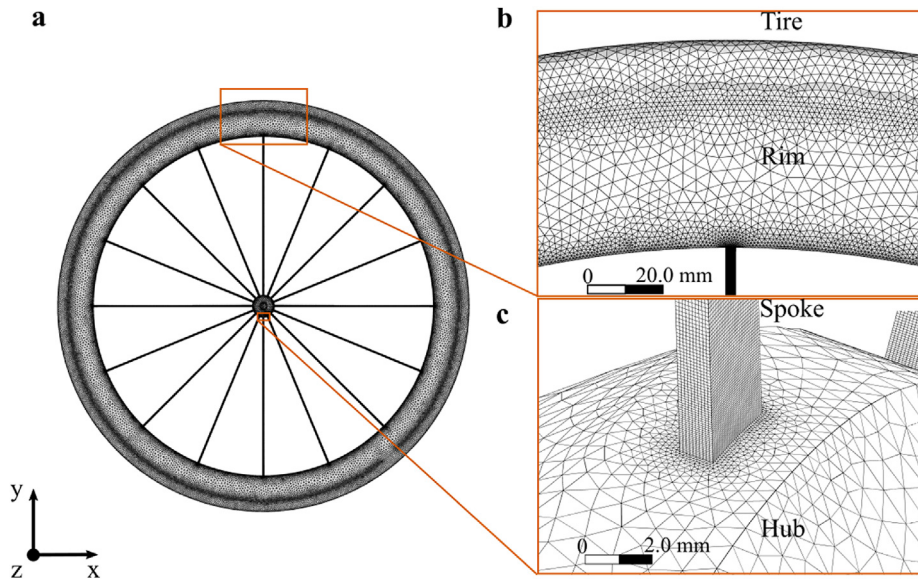


Fig. 6. (a) Wheel surface grid in side view. Surface grid details of (b) tire - rim and (c) spoke - hub.

inlet velocity of 13.41 m/s. The dimensionless distance, y^+ , is defined as:

$$y^+ = \frac{u^* y}{\nu} = \sqrt{\frac{\tau_w}{\rho}} \frac{y}{\nu} \quad (2)$$

where u^* is the friction velocity, y the distance of the cell center point to

the wall, ν the kinematic viscosity and τ_w the wall shear stress. The number of prismatic layers is set to 24 and a last-ratio approach is used to ensure a smooth transition between the prismatic cells and the tetrahedral cells. The last-ratio approach refers to the ratio between the height of the cells in the last prism layer and the size of the local surface-cell where the prisms are being grown from. Therefore, in this approach the growth

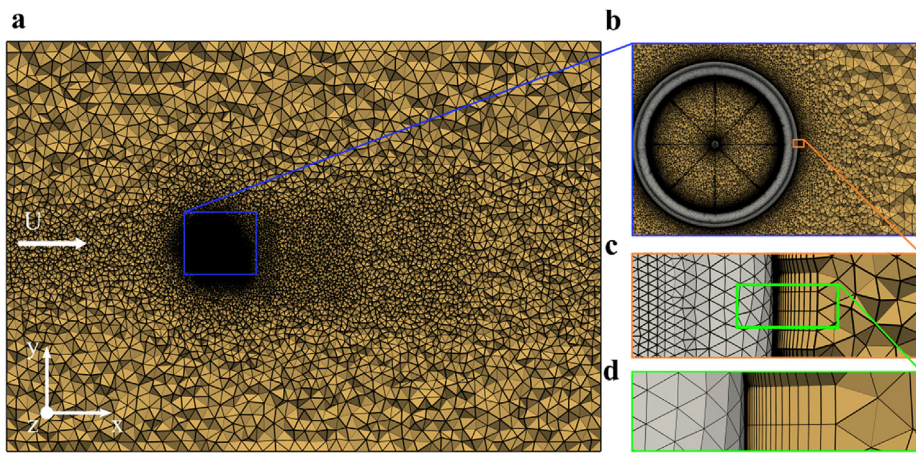


Fig. 7. Volume grid slices at the centerplane $z = 0$ showing: (a) the entire domain; (b) the wheel; (c–d) details of the prism layers at the tire.

rate is computed locally and it is a function of the surface-cell size. In this study, the last-ratio is set as 40% of the surface cell. The impact of the near-wall grid is investigated in detail in Section 5.2.

The far-field grid with tetrahedral cells is generated by applying seven different body-of-influence (BOI) size functions: these BOIs are located in front, around and in the wake of the wheel, as shown in Fig. 8. Inside these BOIs, the maximum grid size is limited and a growth rate is used to define the maximum size difference between two consecutive cells. The maximum cell size is set to be 100 mm in the front BOI, 30 mm around the wheel, 20 mm in the wheel lower half and 50 mm, 75 mm, 100 mm and 150 mm in the four BOIs located in the wheel's wake, respectively. A cell growth rate of 1.10 is applied in all the BOIs of this reference grid, whereas a cell growth rate of 1.20 is applied in the rest of the domain. The cell count in the entire grid is about 30.3 million. The sensitivity analysis for the far-field volume grid will be discussed in Section 5.3.

4.3. Boundary conditions and computational settings

A uniform approach-flow velocity ($U = 13.41 \text{ m/s}$) and turbulence intensity ($\text{TI} = 0.4\%$) profile is used at the inlet boundary, in line with the

experiment by Tew and Sayers (1999). The inlet specific dissipation rate ω is computed from the turbulence intensity and the hydraulic diameter. The latter is set to 0.696 m, based on the jet dimensions used in the experiment. Zero static gauge pressure is used at the outlet boundary while symmetry boundary conditions are used at the lateral, top and bottom faces of the domain (Fig. 5). The rotational velocity inside the MRF volume is set equal to 38.32 rad/s, based on the inlet wind velocity and the wheel diameter, and identical to the value by Tew and Sayers (1999). The wheel surface roughness was assumed to be zero, which is a common simplification in cycling aerodynamics (e.g. Beaumont et al., 2018; Blocken et al., 2018a, 2018b; Griffith et al., 2014; Mannion et al., 2018a).

The commercial CFD code ANSYS/Fluent 18.2 is used to perform the simulations (ANSYS inc, 2017a). The 3D RANS equations are solved together with the $k-\omega$ SST turbulence model. The RANS approach is the common approach for studies on cycling aerodynamics and has been shown to provide close agreement with WT measurements provided that proper computational parameters are applied (e.g. Beaumont et al., 2018; Blocken et al., 2016, 2018c; Fintelman et al., 2015; Griffith et al., 2014; Mannion et al., 2018a, 2018b). Note that no wall models are used but

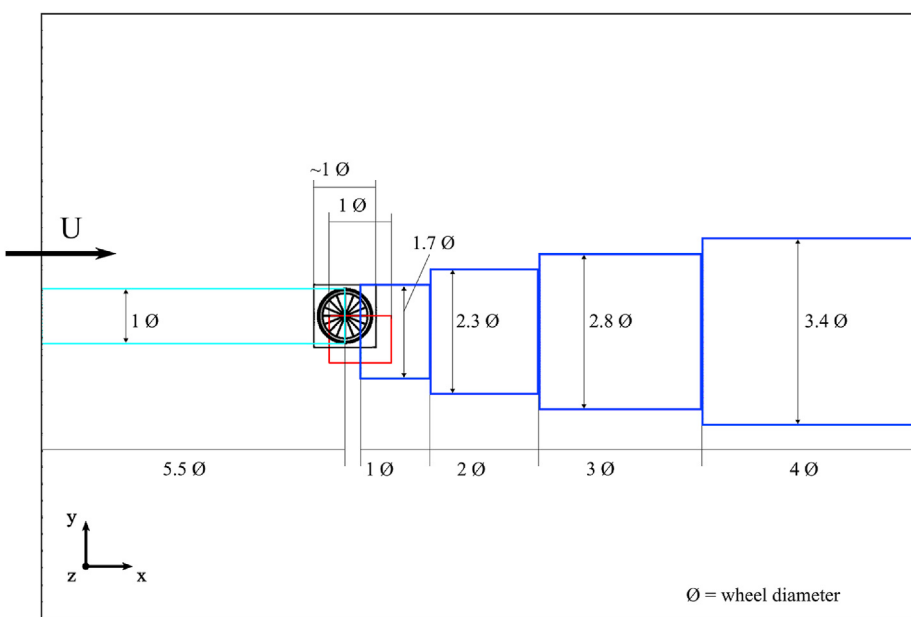


Fig. 8. Bodies of influence (BOIs) used during the volumetric grid creation. Cyan line indicates the BOI in front of the wheel, black line the BOI around the wheel, red line the BOI used to refine the volume in the wheel bottom half and the blue lines for the BOIs in the wake. Some BOIs are asymmetrical because of wheel rotation direction. (For interpretation of the references to colour in this figure legend, the reader is referred to the Web version of this article.)

that instead a low-Reynolds number modeling approach is adopted in which the thin viscous sub-layer is completely resolved. The sensitivity of the simulation results to the turbulence model will be investigated in Section 7. The Coupled algorithm is used for the pressure-velocity coupling together with the pseudo-transient under relaxation. The pseudo time-step is computed using the equation provided in the ANSYS Fluent theory guide (ANSYS inc, 2017b) for cases with rotational velocities:

$$\Delta t_{pt} = \frac{0.1}{\omega} = 2.61 \cdot 10^{-3} \text{ s} \quad (3)$$

Aerodynamic drag and momentum are averaged over the last 10,000 pseudo time steps from a total of 12,000. The gradients are obtained using the Green-Gauss node-based scheme, while pressure interpolation is second-order. All equations are discretized with the second-order upwind scheme. The maximum values for the scaled residuals were: 2×10^{-4} for continuity, 5×10^{-6} for momentum, 8×10^{-4} for turbulent kinetic energy, 3×10^{-4} for specific dissipation rate.

4.4. CFD results and validation with wind tunnel experiments

The computed drag coefficient for the reference case is 0.0273, which is about 15.7% larger than the experimental value, equal to 0.0236 ± 0.0005 . This does not represent an acceptable agreement. In the next sections, it will be shown why this deviation is this larger and how it can be remediated. The computed rotational moment coefficient is equal to 0.0151, but no experimental value is available for this quantity.

5. Impact of the computational grid

In this section, a sensitivity analysis is performed to investigate the impact of the surface grid, the near-wall volume grid (prism layers) and the far-field volume grid on the simulation results. For all these simulations, the MRF approach is used to model the wheel rotation, and the k- ω SST turbulence model is employed. The evaluation is based on

aerodynamic force and rotational moment coefficients, and on the pressure coefficient distribution along the tire centerline.

5.1. Impact of the surface grid

The impact of the surface grid is investigated in two steps. First, the grid on the spokes is systematically refined while the grid resolution for the other components remains almost identical to that of the reference case: the surface cells on the hub and the rim in the vicinity of the spokes are adjusted in size to ensure a smooth transition between the surface cells (Fig. 9). In the second step, the grid resolution on the spokes remains unchanged, while the surface grids for the rim, tire and hub are systematically refined (Fig. 12).

5.1.1. Impact of the spoke surface grid

The impact of the surface grid on the spokes is investigated using seven different grids (Fig. 9). The cell size along the spoke edge varies from 0.1 mm to 0.5 mm, thus 10 to 2 cells are used along the shorter edge of the spoke (1 mm length). These grids are sequentially named Spk1 (0.1 mm surface cell size) to Spk7 (0.5 mm surface cell size). The Spk1 grid (reference case described in Section 4.2) is used as the reference grid during this analysis. The use of different cell sizes on the spoke surface has a large impact on the total cell count of surface grid (Fig. 10a) and of the volume grid (Fig. 10b). It can be seen that the total number of cells decreases significantly when the cell size increases from 0.1 mm (reference case) to 0.2 mm (Spk4): -66% and -54% for surface and volume grid, respectively (Fig. 10).

The results are presented in terms of drag and rotational moment coefficients (Fig. 11). It can be seen that coarsening the grid leads to an increase in both the drag and rotational moment coefficients. This increase is more pronounced for the cell sizes equals or greater than 0.2 mm (Spk4). For example, by coarsening the cell size from 0.1 mm (Spk1) to 0.5 mm (Spk7), the drag and rotational moment coefficients increase by about 4.8% and 13.5%, respectively. For the case with cell size equal to 0.167 mm (Spk3), these drag and rotational moment coefficients increases

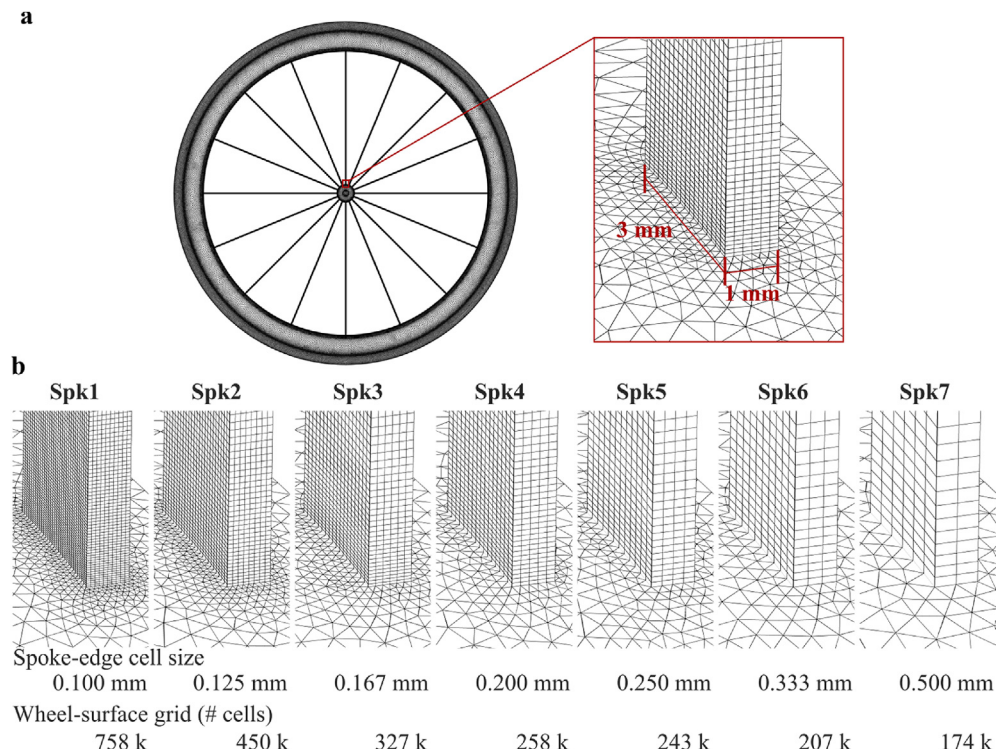


Fig. 9. (a) Surface grid at the spoke, including spoke dimensions; (b) different cases considered, with a spoke-edge cell size varying between 0.1 mm and 0.5 mm. “k” is used for thousands (10^3).

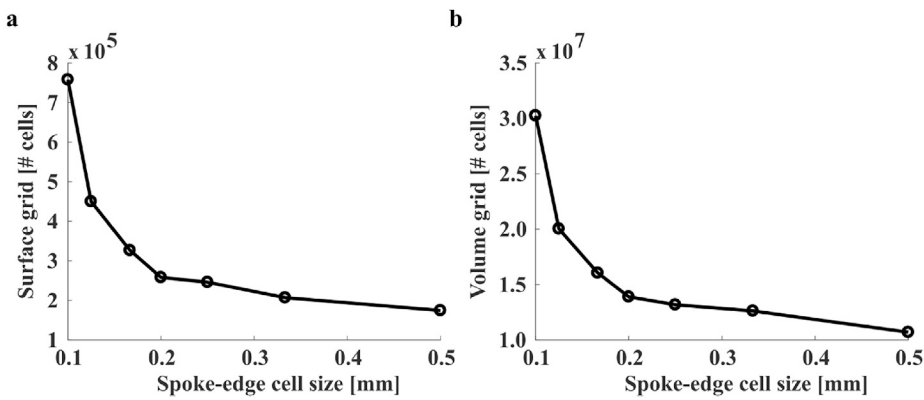


Fig. 10. Decrease in (a) surface grid cell count and (b) volume grid cell count when increasing the spoke-edge cell size.

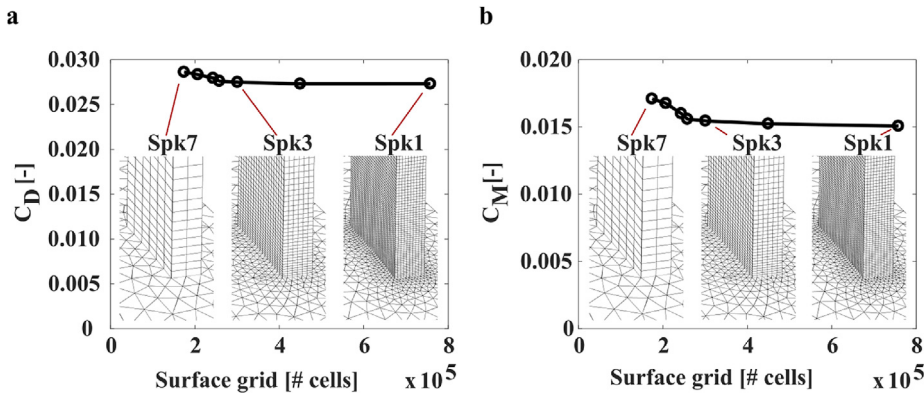


Fig. 11. Impact of the spoke-edge size on (a) the drag coefficient; and (b) the rotational moment coefficient.

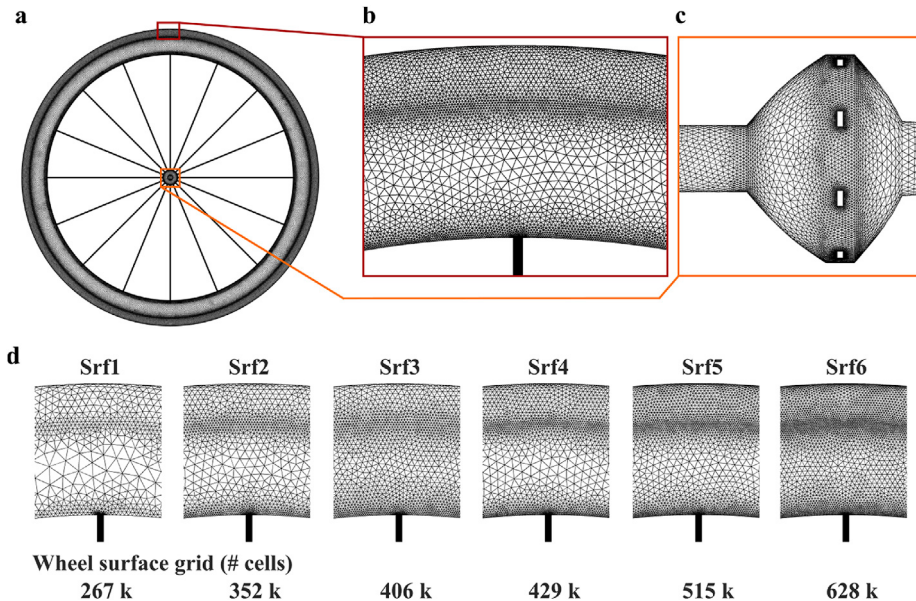


Fig. 12. Surface grid of (a) entire wheel; (b) rim and spoke; (c) hub; (d) different cases analyzed in the wheel surface-grid sensitivity analysis. The spoke grid is the same for each case and follows the previous Spk5 grid. “k” is used for thousands (10^3).

are about 0.7% and 2.6%, respectively, while the total number of cells decreases by 47%. Therefore, the Spk3, with cell edge size along the spoke circumference of 0.167 mm, is chosen for the second step of this study.

5.1.2. Impact of rim, tire and hub surface-grid

In this section, the surface grid on the rim, tire and hub is

systematically varied while the surface grid on the spokes is kept identical to Spk3 used in Section 5.1.1. Six grids are created with surface grid cell counts ranging from 267 k to 628 k cells (Fig. 12), sequentially named Srf1 to Srf6.

Fig. 13 presents the results of the drag and rotational moment coefficients for the different grids. By coarsening the grid, the drag

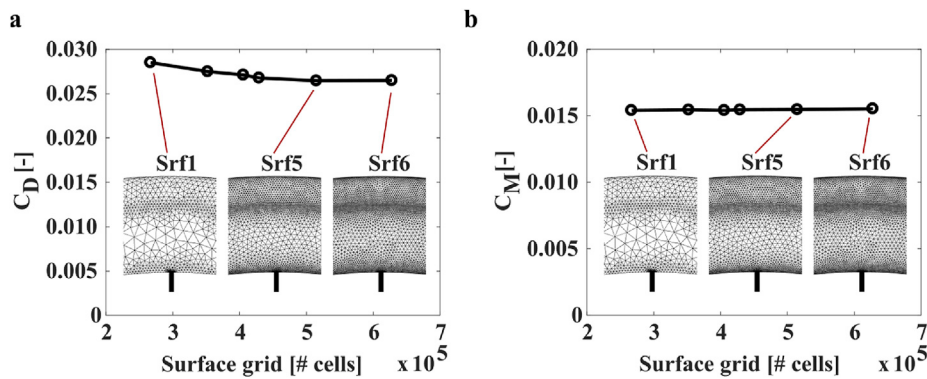


Fig. 13. Impact of the wheel surface-grid size on (a) the drag coefficient; and (b) the rotational moment coefficient.

coefficient increases monotonically, while no significant variation can be seen for the rotational moment. For example, compared to the grid with the largest number of cells, Srf6, the C_D increases by about 7.6% and 1.1% for Srf1 and Srf4, while the C_M reduction is about 0.8% and 0.5%, respectively. These deviations reduce to 0.1% and 0.4% for C_D and C_M , respectively, when the grid Srf5 is compared to the grid Srf6.

To better explain these deviations, Fig. 14 compares the pressure coefficient, C_p , at the tire centerline for four grids, Srf1, Srf3, Srf5, Srf6. The pressure coefficient is defined as:

$$C_p = \frac{P - P_\infty}{0.5\rho U^2}$$

where P and P_∞ are the static pressure at the point of interest and the unperturbed static pressure at the inlet. A C_p value of one is associated with stagnating flow, and it is found at around 0° , where $\theta = 0$ is the most forward point of the tire centerline. With increasing θ , the C_p decreases until a bump occurs at around $\theta = 90^\circ$. At the rear of the wheel, the C_p is almost constant, which is indicative of a separated flow region (Fackrell, 1974). The highest deviations between the coarsest grids (Srf1 and Srf3) and the finest grid (Srf6) are found in the front and lower part of the wheel where θ ranges between 340° and 160° , while almost no deviations are present in the back and upper part of the wheel. In addition, the C_p profiles for Srf5 and Srf6 are almost identical for the entire wheel circumference, confirming that near-grid independence is found for the

drag and rotational moment coefficient for these grid resolutions (Fig. 13). Therefore, Srf5 grid is retained as surface grid for further analysis.

5.2. Impact of near-wall volume grid

In this section, the impact of the near-wall volume grid (or prism layers) is investigated. These layers are of particular importance since a low-Reynolds number modeling approach for the resolution of the RANS equations is used. In this approach, the grid near the wall needs to include cells embedded within the viscous sub-layer; i.e. the region where the dimensionless normal-to-wall distance (y^+) is smaller than 5. In this near-wall grid, only hexahedral cells and wedge cells are used. The use of these two different cell types is needed since both quadrilateral and triangular cells are used on the wheel surfaces.

The near-wall grid layers are generated using the last-ratio approach. The last-ratio is set to 40% to ensure a smooth transition between the wedge/hexahedral cells and tetrahedral cells, which are used in the far-field volume grid. The near-wall volume grid is first studied by varying the height of the wall-adjacent cell, thus the y^+ . Afterwards, the impact of the number of prism layers is investigated.

5.2.1. Impact of y_1 and y^+

Four grids are created to investigate the impact of the y^+ value on the

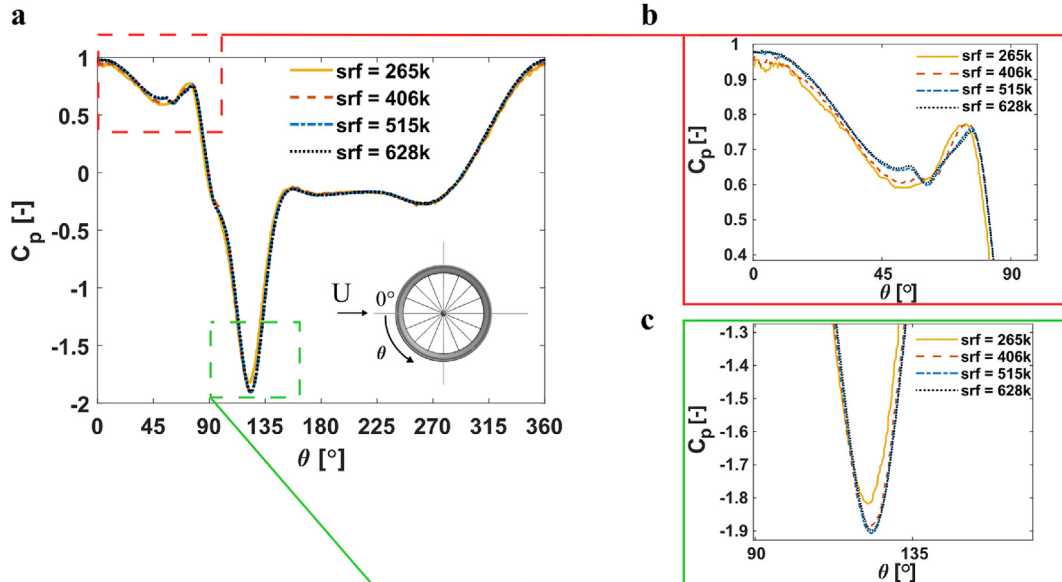


Fig. 14. (a) Pressure coefficient along the tire centerline for four different surface grids; close-views near the locations with higher discrepancies: (b) between 0° and 100° (c) between 90° and 170° .

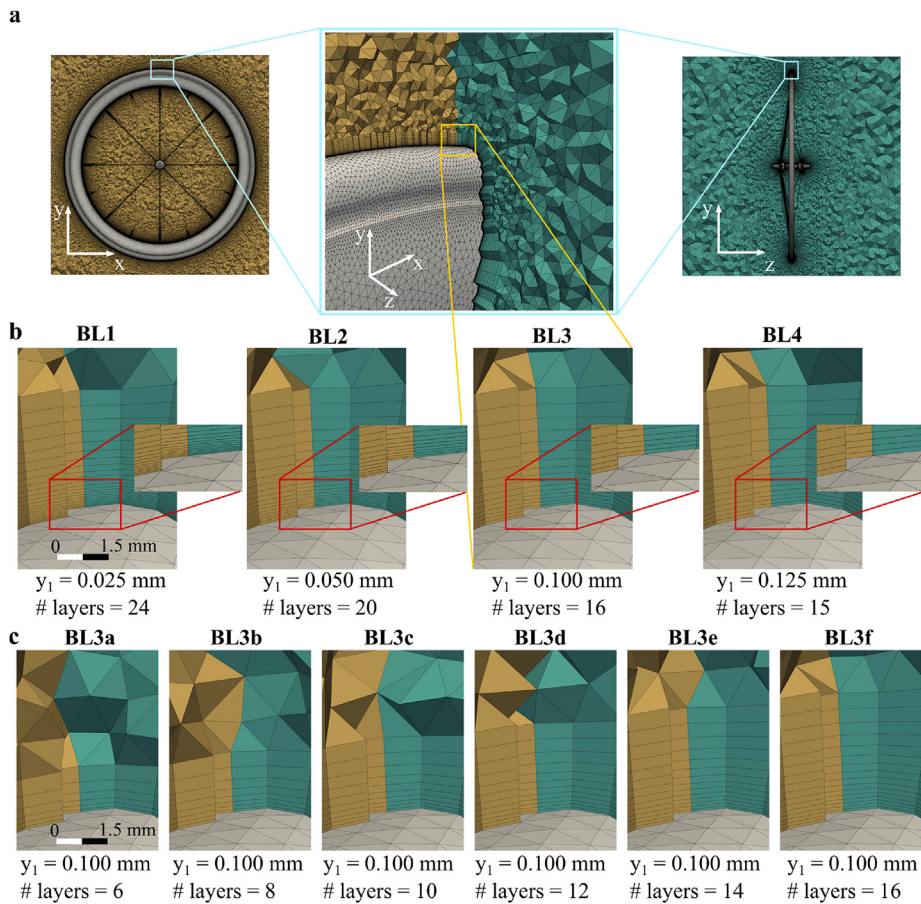


Fig. 15. (a) Slices of volume grid in side (yellow), perspective, and front view (green). The perspective view is zoomed in on the top of the wheel near the tire; (b) grid details of the four cases used for the sensitivity analysis related to the height of the wall-adjacent cell, y_1 ; (c) grid details of the six cases used for the sensitivity analysis related to the number of prism layers. The height of the wall-adjacent cell is set as in grid BL3. (For interpretation of the references to colour in this figure legend, the reader is referred to the Web version of this article.)

results. The height of the wall-adjacent cell, y_1 , is 0.025 mm (BL1), 0.050 mm (BL2), 0.100 mm (BL3) and 0.125 mm (BL4), as shown in Fig. 15b. These heights correspond to an average y^+ variation from 0.9 (BL1) to 4.4 (BL4), whereas the maximum y^+ ranged from 2.5 (BL1) to 8.8 (BL4). Note that the local maximum y^+ of 2.5 is different from the 2.6 value of the reference case (section 4.2) because of the different wheel surface grid of the two cases. Moreover, note that the number of prism layers is varied for the four cases, from 24 (BL1) to 15 (BL4), to keep approximately the same prism layer height on the top of the wheel tire, which is chosen as reference point to compare the prism layer height (Fig. 15a). At this location, the prism layer height is about 4.5 mm.

The results are shown in Fig. 16. Considering the model with the smallest average y^+ (= 0.9) as reference (BL1), the drag is underestimated by 0.1% and 1.7% for the cases with an average y^+ value of 3.5

(BL3) and 4.4 (BL4), respectively. For these two grids the maximum y^+ is 7.4 (BL3) and 8.8 (BL4). The rotational moment, however, shows less sensitivity to the y^+ variations. C_M is overestimated by about +0.3% for BL3, while no variation is observed for BL4. Therefore, the BL3 grid with $y_1 = 0.1 \text{ mm}$ (and 16 prism layers) is considered in the remainder of the analysis.

5.2.2. Impact of the number of prism layers

In this section, the height of the wall-adjacent cell, y_1 , is kept equal to 0.100 mm (average $y^+ = 3.5$) while the number of prism layers is varied sequentially from 6 (BL3a) to 16 (BL3f), in intervals of two layers for a total of six grids (Fig. 15c). Note that the different number of prism layers also affects the total prism layer height.

Fig. 17 shows the impact of the number of prism layers on the drag

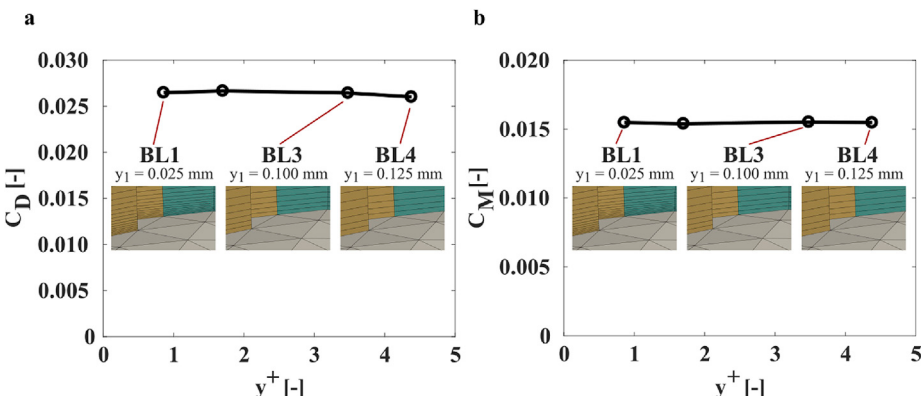


Fig. 16. Impact of the height of the wall-adjacent cell on (a) the drag coefficient; and (b) the rotational moment coefficient.

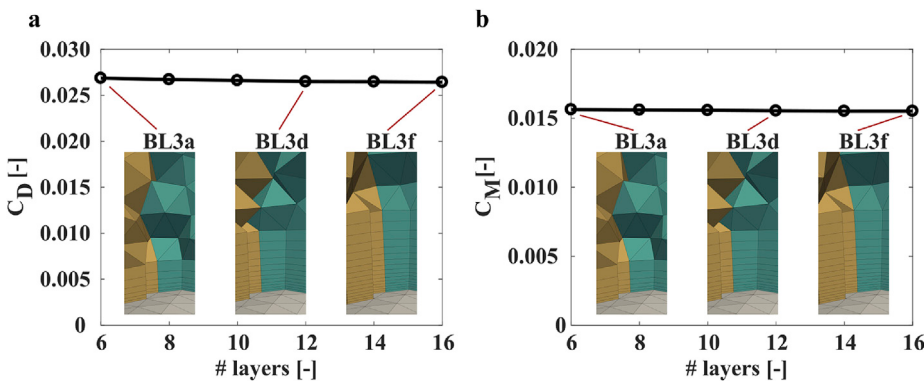


Fig. 17. Impact of the number of prism layers on (a) the drag coefficient; and (b) the rotational moment coefficient.

and rotational moment. By decreasing the number of prism layer from 16 (BL3f) to 6 (BL3a), the drag and rotational moment increase by about 1.6% and 0.7%, respectively. It should be noted that in this case the number of cells in the prism layers decreases by more than 60%. A closer look at this figure reveals that 12 prism layers seem to be sufficient to ensure that the results are nearly independent of this aspect of the computational grid since a further increase of the number of cells will not have any significant impact on the results: the drag and rotational moment coefficients increase by only 0.2% and 0.1% when the number of prism layers decreases from 16 to 12. Therefore, the BL3d grid, with 12 prism layers, is used for the following analysis concerning the impact of the far-field volume grid.

5.3. Impact of the far-field volume grid

The far-field volume grid includes tetrahedral cells and pyramidal cells where the latter are present to provide a transition from the near-wall hexahedral cells located around the spokes and the far-field tetrahedral cells. The far-field tetrahedral cells are created using several body-of-influence (BOIs) size functions, as previously shown in Fig. 8. The cell size is limited in these BOIs, while a smooth cell size transition is guaranteed by a growth rate equal to 1.2 in the rest of the domain.

Six different grids are created varying only the cell growth rate inside these BOIs. The grids are sequentially named from Vol1, the coarsest grid with a cell growth rate of 1.20, to Vol6, the finest grid with a growth rate of 1.05. Fig. 18c presents the growth rate of cells together with the total number of cells, which ranges from 12.7 M cells (Vol1) to 45.7 M cells (Vol6).

The results are shown in Fig. 19. It can be observed that the deviations between the drag and rotational moment coefficients obtained by the finest grid (Vol6) and the coarsest grid (Vol1) are about +1.8% and -1.4%, respectively. For the Vol2 grid, these deviations are +0.6% and -1.4%, respectively. In this case, the total number of cells compared to the finest grid reduces by about 68%. Therefore the Vol2 grid, with the maximum growth rate fixed to 1.15 in the BOIs, is retained for further analyses.

6. Impact of rotational modeling

This section presents the sensitivity of the simulation results to the wheel rotational modeling. The evaluation consists of three parts:

- 1) Impact of the size of the MRF volume: a cylindrical MRF volume is considered and the impact of different sizes of this MRF volume is evaluated. In this case the MRF approach is used to model the wheel rotation;
- 2) Impact of the shape of the MRF volume: three different MRF volume shapes are considered, cylindrical, rounded and frustum. The MRF approach is used to model the wheel rotation;

- 3) Impact of rotational approach: three approaches are considered to model the wheel rotation (Fig. 20), namely (i) rotating wall boundary condition (RW), (ii) moving reference frame (MRF) applied on a volume surrounding the entire wheel, and (iii) hybrid MRF-RW, with the MRF applied on a volume surrounding the inner wheel (hub, spokes and inner rim) and the RW applied on the outer wheel (outer rim and tire).

In the RW approach (Fig. 20a), a velocity term is applied directly to the wheel boundary faces. Contrarily, in the MRF approach (Fig. 20b), the rotation is applied in a fluid zone surrounding the wheel and separated from the outer fluid region by an interface. This approach is based on considering different reference frames for each part of the fluid: the rotational effects are included in the inner region through four additional terms in the momentum equation. These terms reduce to two when no rotational accelerations are present: the Coriolis acceleration and the centripetal acceleration (ANSYS inc, 2017b). These two terms can be expressed, using a velocity formulation relative to the moving reference frame, as:

$$\text{Coriolis acceleration} = 2 \vec{\omega} \times \vec{v}_r \quad (4)$$

$$\text{Centripetal acceleration} = \vec{\omega} \times \vec{\omega} \times \vec{r} \quad (5)$$

where $\vec{\omega}$ and \vec{v}_r are the angular velocity and the relative velocity viewed from the moving frame, respectively, while \vec{r} is the distance of a cell from the origin of the moving frame.

The last approach, the MRF-RW (Fig. 20c), is a hybrid approach where the MRF is applied inside a volume surrounding the inner part of the rim, the spokes and the hub, while the RW is applied on the outer part of the rim and the tire.

6.1. Impact of the MRF volume size in the MRF rotational approach

In this section, the impact of the size of the MRF volume is investigated. Eight cases are considered (Fig. 21) in which cylindrical MRF volumes are used. The change in the size of the volumes is obtained by changing the distance “s” between the MRF volume faces and the wheel-ends (Fig. 21). The distance “s” varies from $s = 7.5$ mm (Cyl1) to $s = 50.0$ mm (Cyl8). As the rotational accelerations are applied in the entire MRF volume, the case with the smallest volume (Cyl1), whose faces are closer to the wheel than the other cases, is used as a reference.

The impact of the size of the MRF volume on the computed drag and rotational moment is provided in Table 3. Increasing the MRF volume size leads to an increase in both drag and rotational moment coefficients. Compared to Cyl1 ($s = 7.5$ mm), the use of Cyl8 ($s = 50.0$ mm) leads to an overestimation of about 8.5% and 2.6% in the predicted drag and rotational moment coefficients, respectively. These deviations are equal to and less than 0.4% for the drag and rotational moment

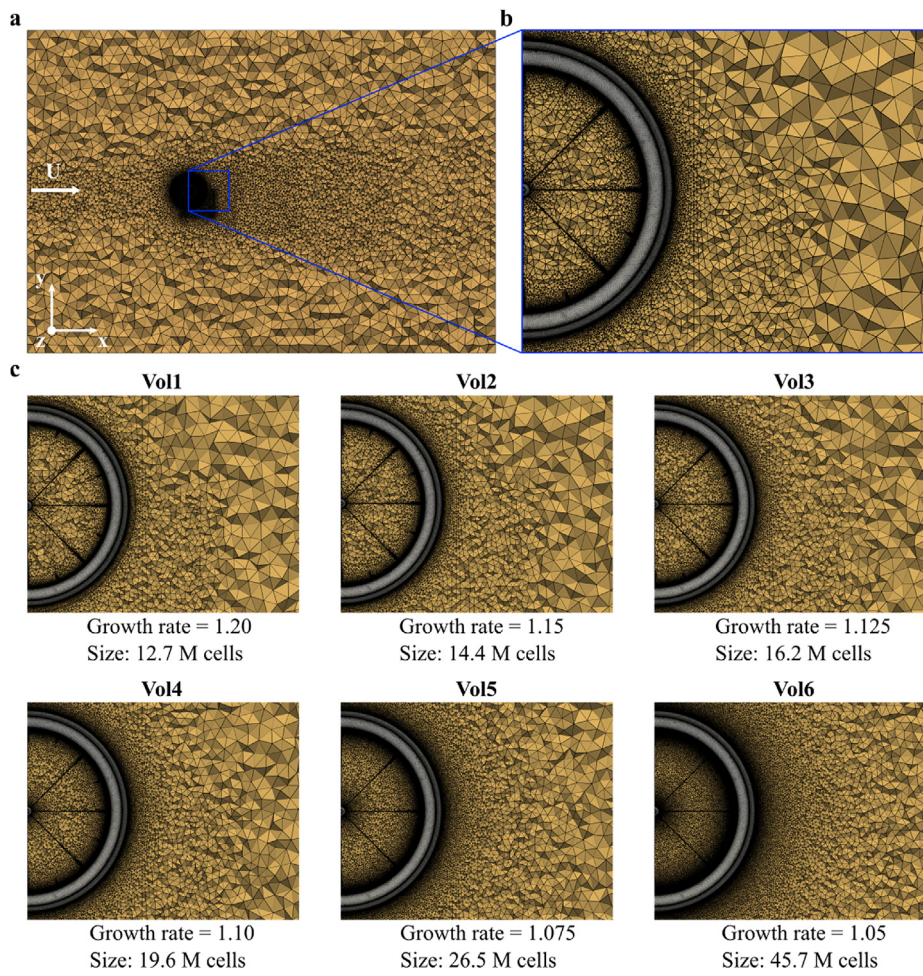


Fig. 18. (a) Volume grid in the wheel symmetry plane for the case with growth rate = 1.15; (b) zoom of the volume grid near the wheel's rear part; (c) volume grid for the six different cases analyzed in the volume grid sensitivity analysis. “M” is used for millions (10^6).

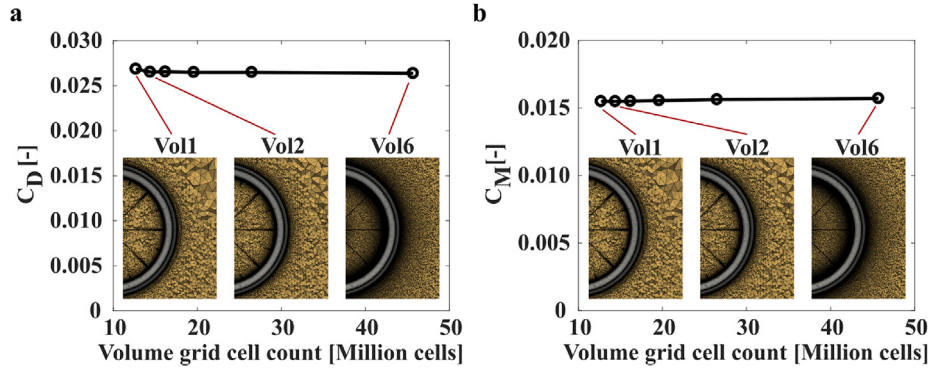


Fig. 19. Impact of the volume grid cell count on (a) the drag coefficient; and (b) the rotational moment coefficient.

coefficients, respectively, when using the MRF volume with $s = 10.0$ mm (Cyl2).

Fig. 22 shows the pressure coefficient along the tire centerline. Four cases are considered: Cyl1 ($s = 7.5$ mm), Cyl2 ($s = 10.0$ mm), Cyl4 ($s = 15.0$ mm) and Cyl8 ($s = 50.0$ mm). It can be observed that for θ between 340° and 160° (front-bottom section) the size of the MRF volume has a significant impact of the C_p , while for θ between 160° and 340° (rear-top section) this impact is rather smaller. This is clear considering the case with the largest distance “ s ” analyzed, Cyl8 ($s = 50.0$ mm), which presents an earlier and larger pressure peak at about 65° and a

larger pressure dip at about 120° , while small differences are found in the rear-top wheel section. The impact of the MRF volume size on the C_p results reduces for closer distances s , like Cyl2 with $s = 10.0$ mm, and a good agreement is found between Cyl1 and Cyl2 in terms of computed drag and rotational moment.

This analysis shows that the MRF volume does have an impact on wheel aerodynamics and that small MRF volumes should be selected, with a suggested distance $s \leq 10.0$ mm. Moreover, the C_p analysis shows the regions of the flow where the MRF volume size has the largest impact: in front and below the wheel.

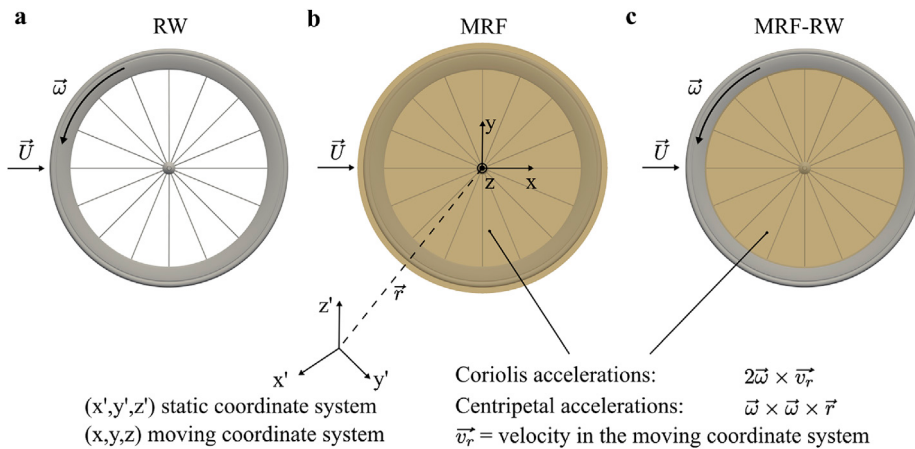


Fig. 20. Different rotational approaches: (a) rotating wall (RW); (b) moving reference frame (MRF); (c) hybrid MRF-RW.

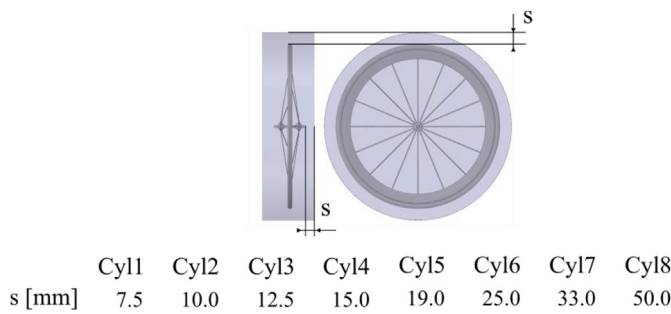


Fig. 21. Definition of the distance "s" used to build the MRF volume.

6.2. Impact of the MRF volume shape in the MRF rotational approach

Three different shapes are considered: (i) cylindrical; (ii) cylindrical with rounded edges (rounded) and (iii) frustum (Fig. 23). To better generalize the results, also the size of the MRF shapes is studied here for the rounded and frustum cases. Different cases are considered for $s = 10.0 \text{ mm}, 12.5 \text{ mm}, 25 \text{ mm} \text{ and } 50 \text{ mm}$.

Fig. 24 shows the drag and rotational moment coefficient for the three MRF volume shapes as a function of the distance "s". It can be seen that both rounded and frustum shaped MRF volumes, compared with the cylindrical MRF volume, underestimate the drag coefficient for all values of "s" with the exception of the frustum case with $s = 10.0 \text{ mm}$. For the rounded cases, this underestimation varies from 3.6% for $s = 50 \text{ mm}$ to 0.5% for $s = 10.0 \text{ mm}$. For the frustum case, however, this underestimation is more pronounced and reaches about 13.0% for the largest MRF volume ($s = 50 \text{ mm}$), while a 1.0% overestimation is obtained for the smallest MRF volume with $s = 10.0 \text{ mm}$. It is worth to note that when $s = 12.5 \text{ mm}$, the drag coefficient for both rounded and frustum shapes is very close to that obtained when the cylindrical shape is used, -1.1% and -1.0%, respectively.

Fig. 24b indicates that the shape of the MRF volume has no significant impact on the rotational moment for all values of "s". For example, for $s = 10.0 \text{ mm}$ and 12.5 mm , the deviation between the rounded and cylindrical MRF is about 0.1% and 0.2%, respectively. For the cylindrical and frustum shaped MRF volumes, the deviation is about 1.7% and 1.5%,

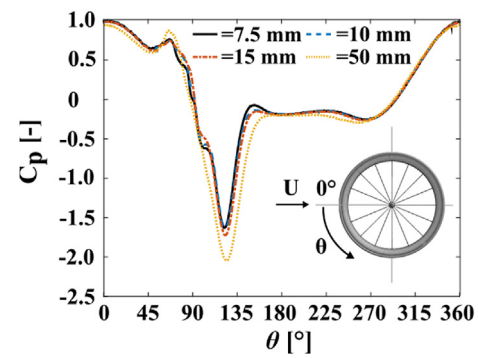


Fig. 22. Pressure coefficient along the tire centerline for four different MRF volumes.

respectively.

The impact of the MRF shape is further investigated by means of contour plots of the vertical component of velocity (y -direction) non-dimensionalized with the freestream velocity U , in two planes for the three MRF volume shapes with $s = 12.5 \text{ mm}$ (Fig. 25). The planes are located at a distance of $\phi/4$ and $\phi/2$ from the hub center (Fig. 25a) in the wake direction. Similar velocity distributions can be seen for the cylindrical and rounded MRF volumes. The use of the frustum-shaped MRF, however, leads to significant differences in the velocity distribution for both planes. This is especially the case for the lower part of the planes where rather high velocity gradients are observed: the wide portion of fluid with high negative vertical velocity present when cylindrical and rounded MRF volume shapes are used, is reduced in width when the frustum MRF volume shape is used.

In conclusion, the MRF volume shape has an impact on the computed aerodynamic drag and rotational moment. Volumes with inclined surfaces (frustum) should be avoided in favor of volumes with cylindrical shape or rounded shape. The latter shape was created using a cylindrical shape with rounded edges.

6.3. Impact of rotational approach

Three rotational modeling approaches (Fig. 20), are investigated:

Table 3
Impact of the MRF volume size on drag and rotational moment coefficients.

Case	Cyl1	Cyl2	Cyl3	Cyl4	Cyl5	Cyl6	Cyl7	Cyl8
t [mm]	7.5	10.0	12.5	15.0	19.0	25.0	38.0	50.0
$C_D [-]$	0.0258 (Ref.)	0.0259 (+0.4%)	0.0261 (+1.2%)	0.0263 (+1.9%)	0.0265 (+2.7%)	0.0265 (+2.7%)	0.0272 (+5.4%)	0.0280 (+8.5%)
$C_M [-]$	0.0153 (Ref.)	0.0153 (+0.0%)	0.0153 (+0.0%)	0.0153 (+0.0%)	0.0154 (+0.7%)	0.0155 (+1.3%)	0.0156 (+2.0%)	0.0157 (+2.6%)

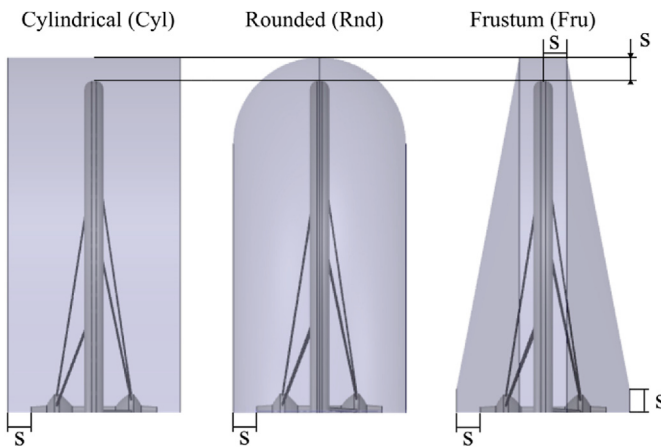


Fig. 23. Three different shapes for MRF approach.

- 1) rotating wall boundary condition applied to the entire wheel (RW);
- 2) moving reference frame approach applied on a volume surrounding the entire wheel (MRF);
- 3) hybrid MRF and RW (MRF-RW) with MRF applied to a volume that surrounds only the spokes, the hub and the inner rim section, while the RW boundary condition is applied on the outer rim section and the tire.

In addition, the impact of the MRF volume size on the wheel aerodynamics is also investigated when the hybrid MRF-RW approach is used to model the wheel rotation, similar to what was done in subsection 6.1 where the MRF approach was used to model the wheel rotation. Once the impact of this parameter is investigated, it will be possible to compare the

results obtained using the three aforementioned rotational approaches. Therefore, the inner MRF volume size dependence to the results is discussed first (subsection 6.3.1), after which the results obtained with the different approaches are compared and evaluated against wind tunnel tests (subsection 6.3.2).

Note also that the rotating wall boundary condition correctly reproduces the tangential rotational motion only when applied to walls bounding surfaces of revolution (ANSYS inc, 2017a), which is not the case for the spokes.

6.3.1. Impact of the MRF volume size in the MRF-RW rotational approach

In the MRF-RW approach, the MRF volume surrounds the wheel only partially, specifically the hub, spokes and partially the rim. Four different models are created, each with a different distance “ t ” from the inner rim edge to the external MRF volume face (Fig. 26). These models are sequentially named Cin1 to Cin4 and the distance “ t ” varies from 5 mm (Cin1) to 35 mm (Cin4) in intervals of 10 mm (Fig. 26). The smaller MRF volume, Cin1 with $t = 5$ mm, is used as reference for all the other cases.

The results in terms of drag and rotational moment coefficients are presented in Table 4. The maximum deviation from Cin1 results is obtained for the largest MRF volume (Cin4) with $t = 35$ mm: drag and rotational moment coefficients are overestimated of 3.9% and 3.5% respectively. The influence of distance “ t ” on the results reduces significantly with the MRF volume Cin2 ($t = 15$ mm); the same drag coefficient as for Cin1 is obtained while the rotational moment coefficient is overestimated by only 0.7%. Therefore a sufficient MRF volume size independence is obtained using small MRF volumes, with $t \leq 15$ mm.

6.3.2. Comparison of different rotational approaches with wind tunnel data

The sensitivity of the results to three rotational approaches is presented in Table 5. The MRF and MRF-RW approaches give drag results that are closest to the WT results (Tew and Sayers, 1999). The deviation is

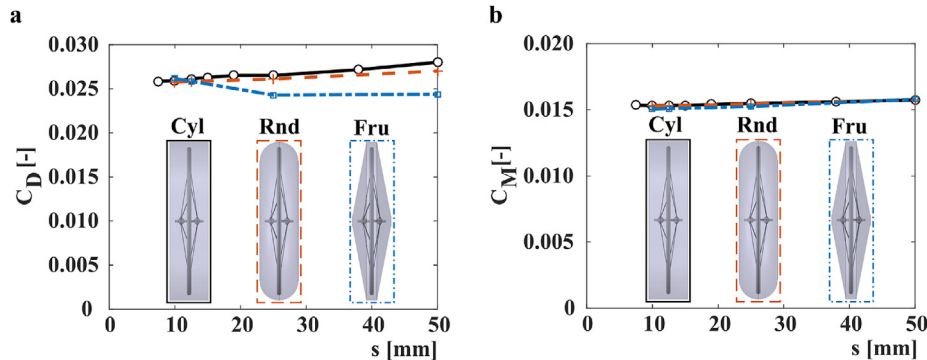


Fig. 24. Impact of the MRF volume shape for different MRF volume sizes, described by the distance “ s ”, on (a) the drag coefficient; and (b) the rotational moment coefficient.

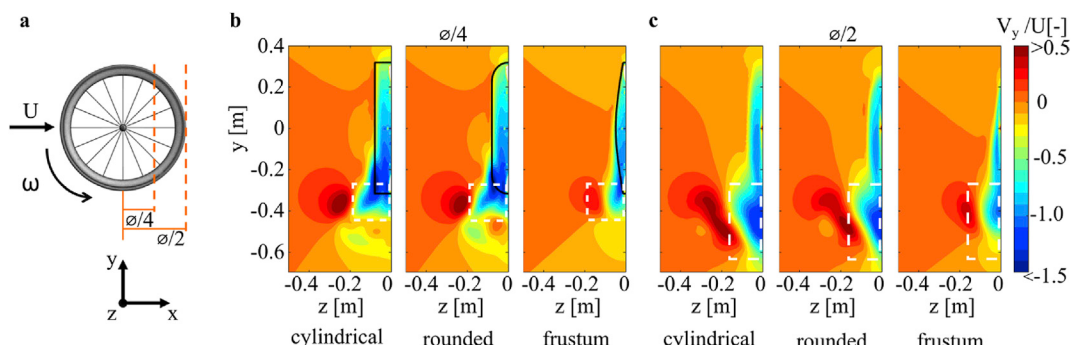


Fig. 25. (a) Definition of the two vertical planes used for the contours. Contours of vertical velocity normalized by approach-flow velocity U , at a distance (b) $\phi/4$; and (c) $\phi/2$ for three different MRF volume shapes with $s = 12.5$ mm. The black lines in b are used to highlight the MRF volume shapes while the white dotted lines highlight the regions of higher discrepancies.

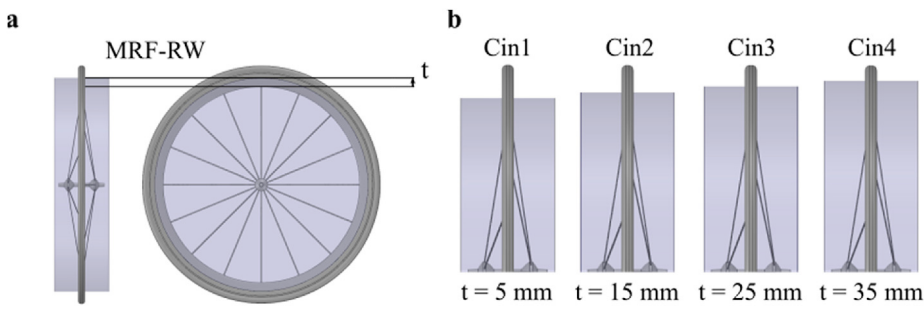


Fig. 26. (a) Definition of distance “ t ” used to characterize the different MRF volumes used in the hybrid MRF-RW approach; (b) four different MRF volumes in the MRF-RW approach.

Table 4

Impact of the inner MRF volume size on the drag and the rotational moment coefficients, when the hybrid MRF-RW approach is used.

Case	Cin1	Cin2	Cin3	Cin4
t [mm]	5	15	25	35
C_D [-]	0.0231 (Ref.)	0.0231 (+0.0%)	0.0234 (+1.3%)	0.0240 (+3.9%)
C_M [-]	0.0142 (Ref.)	0.0143 (+0.7%)	0.0145 (+2.1%)	0.0147 (+3.5%)

Table 5

Impact of rotational approaches on drag and rotational moment coefficients and comparison with wind tunnel results (Tew and Sayers, 1999).

Approach	C_D [-]	C_M [-]
RW	0.0276 (+16.9%)	0.0062
MRF	0.0259 (+9.7%)	0.0153
MRF-RW	0.0231 (-2.1%)	0.0142
Wind tunnel (Tew and Sayers, 1999)	0.0236 ± 0.0005 (ref.)	Not available

-2.1% and +9.7% for the MRF-RW and MRF approaches, respectively. However, the RW approach leads to a rather high deviation of 16.9%. The rotational moment coefficient predicted by the MRF and RW approach is about 7.7% and 56.3% higher and lower than that by the MRF-RW approach, respectively. For this parameter, no WT data were available.

Therefore, it can be concluded that CFD simulation of cycling spoked wheels should be performed using either the MRF or – preferably – the MRF-RW approach.

7. Impact of turbulence modeling

Four RANS turbulence models were considered in this study and selected as follows: one model of the $k-\epsilon$ family which was also used in previous studies of wheel and cycling aerodynamics (Blocken et al., 2016; Pogni and Petrone, 2016); the Spalart-Allmaras turbulence model which was used in previous investigations of cycling wheels (Godo et al., 2009, 2010, 2011); one model of the $k-\omega$ family that generally performs well for cycling and paracycling aerodynamics (Defraeye et al., 2010; Giappino et al., 2018; Mannion et al., 2018b) and one transition model, since at the Reynolds numbers considered the transition might have an impact. Therefore the selected models are: the Spalart-Allmaras model (SA) (Spalart and Allmaras, 1992) with Strain/Vorticity-Based Production, the Realizable $k-\epsilon$ model (Rk- ϵ) (Shih et al., 1995) with enhanced wall treatment, the $k-\omega$ SST model (Menter, 1994) and the $k-\omega$ SST model with intermittency (γ -SST) (Menter et al., 2002). Note that this transition turbulence model has not been developed for complex bluff geometries but it was only calibrated for classical boundary layer flows (ANSYS inc, 2017b) and therefore might not provide substantial added value. The evaluation is performed for both the MRF and the MRF-RW approach in which $s = 10$ mm (Fig. 21) and $t = 5$ mm (Fig. 26). In addition, simulations are

performed using two grids: the grid resulting from the sensitivity analysis in Section 5 (medium grid) and a finer grid. Two reasons drive this choice: (i) to confirm that the grid resulting from the grid sensitivity analysis using the MRF approach for the wheel rotation is also valid when using the MRF-RW approach; (ii) to confirm that the grid resulting from the sensitivity analysis using the $k-\omega$ SST turbulence model is also valid for other turbulence models. The medium grid, thus the grid resulting from the grid sensitivity analysis described in section 5, includes about 515,000 to model the wheel-surface, a height of the wall-adjacent cell of 0.100 mm leading to an average $y^+ \sim 3.5$, 12 prism layers, a wake growth rate of 1.15 and a total cell count of 14.4 M cells. The fine grid includes about 630,000 cells to model the wheel surface, a height of the wall-adjacent cell of 0.025 mm leading to an average $y^+ < 1$, 24 prism layers, a wake growth rate of 1.10 and a total cell count of 29.2 M cells.

The results (Tables 6 and 7), show that the CFD simulations based on the $k-\omega$ SST turbulence model are insensitive to further grid refinement not only when the MRF approach is used for the wheel rotation, as shown in Section 5, but also when the MRF-RW rotational approach is used: -0.4% for the drag coefficient while the same rotational moment coefficient is obtained using the fine grid. The results using the SA and γ -SST turbulence models show a drag coefficient difference between the fine and medium grid smaller than 1% when using the MRF approach, and about 2% when using the MRF-RW approach. In contrast, the simulations with the Rk- ϵ model present a larger grid dependence for both wheel rotational approaches (about 3% for C_D and 1% for C_M).

Comparing the results with the experimental drag coefficient (Tew and Sayers, 1999), a fair agreement is obtained using the MRF approach (Table 6) with the $k-\omega$ SST turbulence model (+9.7%), whereas the other turbulence models yield a larger discrepancy: +11.4% for the Rk- ϵ , +12.7% for the γ -SST and +25.0% for the SA turbulence model, all of them with the fine grid. A good to fair agreement is found using the MRF-RW approach with three different turbulence models: $k-\omega$ SST, γ -SST and Rk- ϵ (Table 7), with a 3.4% maximum error in the drag coefficient. In contrast, CFD simulations with the SA turbulence model over-predict the experimental drag coefficient (+7.2% with the fine grid).

Since no experimental values for the rotational moment coefficient are available for this wheel, only comparisons between the different CFD simulations are possible. The smallest rotational moment coefficient value is obtained for all grids and rotational approaches by the γ -SST turbulence model, which value is generally close to the one obtained using the $k-\omega$ SST turbulence model (+2% to +5% difference) while a higher rotational moment coefficient is obtained using the Rk- ϵ and the SA turbulence models. Nevertheless, the accuracy of the CFD simulations of the rotational moment coefficient cannot be evaluated without additional experimental data.

The impact of the turbulence models on the flow field is investigated by contour plots of the streamwise velocity component (x -direction) non-dimensionalized with the freestream velocity U , in three planes for the four turbulence models and using the fine grid (Fig. 27). The planes are located at a distance of $\varnothing/4$, $\varnothing/2$ and \varnothing from the hub center (Fig. 27a) in the wake direction. The results show small differences among the four

Table 6

Impact of turbulence modeling on drag and rotational moment coefficients and comparison with wind tunnel results (Tew and Sayers, 1999) when using the MRF approach on two grids.

MRF	Medium (M) grid	Fine (F) grid	Ratio Fine/Medium grid	
Turbulence model	$C_D [-] \left(\frac{C_{D,CFD} - C_{D,WT}}{C_{D,WT}} \right)$	$C_M [-]$	$C_D [-] \left(\frac{C_{D,CFD} - C_{D,WT}}{C_{D,WT}} \right)$	$C_M [-]$
SA	0.0297 (+25.8%)	0.0164	0.0295 (+25.0%)	0.0164
Rk-e	0.0274 (+16.1%)	0.0161	0.0266 (+12.7%)	0.0159
k- ω SST	0.0259 (+9.7%)	0.0153	0.0259 (+9.7%)	0.0153
γ -SST	0.0264 (+11.9%)	0.0145	0.0263 (+11.4%)	0.0149
Wind tunnel (Tew and Sayers, 1999)	0.0236 ± 0.0005	Not avail.	0.0236 ± 0.0005	Not avail.

Table 7

Impact of turbulence modeling on drag and rotational moment coefficients and comparison with wind tunnel results (Tew and Sayers, 1999) when using the MRF-RW approach on two grids.

MRF-RW	Medium (M) grid	Fine (F) grid	Ratio Fine/Medium grid	
Turbulence Model	$C_D [-] \left(\frac{C_{D,CFD} - C_{D,WT}}{C_{D,WT}} \right)$	$C_M [-]$	$C_D [-] \left(\frac{C_{D,CFD} - C_{D,WT}}{C_{D,WT}} \right)$	$C_M [-]$
SA	0.0258 (+9.3%)	0.0152	0.0253 (+7.2%)	0.0153
Rk-e	0.0235 (-0.4%)	0.0149	0.0228 (-3.4%)	0.0147
k- ω SST	0.0231 (-2.1%)	0.0142	0.0230 (-2.5%)	0.0142
γ -SST	0.0240 (+1.7%)	0.0136	0.0235 (-0.4%)	0.0139
Wind tunnel (Tew and Sayers, 1999)	0.0236 ± 0.0005	Not avail.	0.0236 ± 0.0005	Not avail.

different turbulence models at the three wake locations considered, with differences mainly localized in the lower half of the wheel and below it, as highlighted with the white boxes in Fig. 27b, c and d. Note also that the contours obtained with the k- ω SST and γ -SST are in very close agreement, in line with the drag coefficient and rotational moment coefficient computed with both turbulence models. It could be argued that the laminar-to-turbulent transition plays a weak role in the cycling wheel aerodynamics, although, as already stated, the γ -SST transition model is not tuned for these complex bluff bodies.

8. Discussion

This study investigates the impact of computational parameters on computed wheel aerodynamics. These computational parameters are the computational grid, the rotational modeling and the turbulence modeling. They are systematically varied and the resulting CFD outcomes are compared each other and with WT experiments available in the literature (Tew and Sayers, 1999). The main limitations of this study are briefly mentioned:

- The spoke shape of the wheel analyzed in this work was approximated with a rectangular cross-section, due to lack of information about its exact shape.
- In this study, only spoked wheel aerodynamics is addressed. Future work should also investigate tri- and four-spoke wheels as well as disc wheels.
- Since the focus of the present paper was to quantify the impact of several computational parameters (i.e. the computational grid size, the wheel rotation modeling and the turbulence modeling) on the cycling wheel aerodynamics, the impact of the wheel-ground contact and crosswind on the wheel aerodynamics were not investigated. Note that Greenwell et al. (1995) reported that: “at low yaw angles the forces on the wheel will be primarily in the axial direction. Taking into account the variation of relative velocity over the wheel (from a minimum at the ground to a maximum away from the ground) the ground effects are likely to be small”. Nevertheless, future research should focus on ground interaction and its impact on the wheel aerodynamics.
- CFD validation is performed by comparing the wheel drag with WT results available in the literature. To the best of our knowledge, no additional WT data are available in the literature on spoked wheels. Present and future research would benefit from additional WT data,

such as mean velocity and pressure fields, which could be used to evaluate the performance of different computational parameters in more detail.

- The CFD simulations were performed for low turbulence level approach flow conditions and they were compared with WT measurements also obtained with low turbulence level approach flow conditions. This is common practice in both WT experiments (e.g. Greenwell et al., 1995; Terra et al., 2019; Tew and Sayers, 1999) and CFD simulations in cycling aerodynamics (Beaumont et al., 2018; Blocken et al., 2018c; Defraeye et al., 2010; Fintelman et al., 2015). However, note that a low turbulence level approach flow might not always be representative of reality and studies on the impact of the turbulence intensity on wheel aerodynamics should be conducted in future.
- In the present analysis, three rotational modeling approaches are used to reproduce the wheel rotation effects without physically rotating the wheel in the simulation. Future work should also investigate the performance of the sliding mesh approach that is widely used in transient simulations, such as car wheel aerodynamics (e.g. Hobeika and Sebben, 2018). In this approach the wheel geometry is physically rotating at every time step.
- Scale resolving CFD simulations, e.g. LES, hybrid RANS-LES and URANS, could provide additional insights on cycling wheel aerodynamics. However, the RANS approach is still the main numerical approach utilized in many aerodynamic applications (Blocken, 2018; Casey and Wintergerste, 2000; Hanjalic, 2005), therefore it has been chosen to focus on this approach in the present study. Note that the proposed guidelines in terms of grid resolution and rotational modeling might also apply to URANS simulations and hybrid RANS-LES, where the RANS equations are solved in the near wall region, however this should be verified by future research.

In addition, note that this paper focuses only on a single isolated wheel. In the past, it has been standard practice in both research and practical engineering for cycling aerodynamics to develop and optimize some components, such as wheels, based on the testing of these isolated components both in wind tunnel experiments and CFD simulations (e.g. Crane and Morton, 2018; Gibertini et al., 2010; Godo et al., 2010; Oggiano et al., 2009; Underwood et al., 2015; Zdravkovich, 1992). Nevertheless it has also been acknowledged that for assessing the final cyclist performance the whole system of cyclist together with all bicycle components should be considered. Indeed previous research has shown that

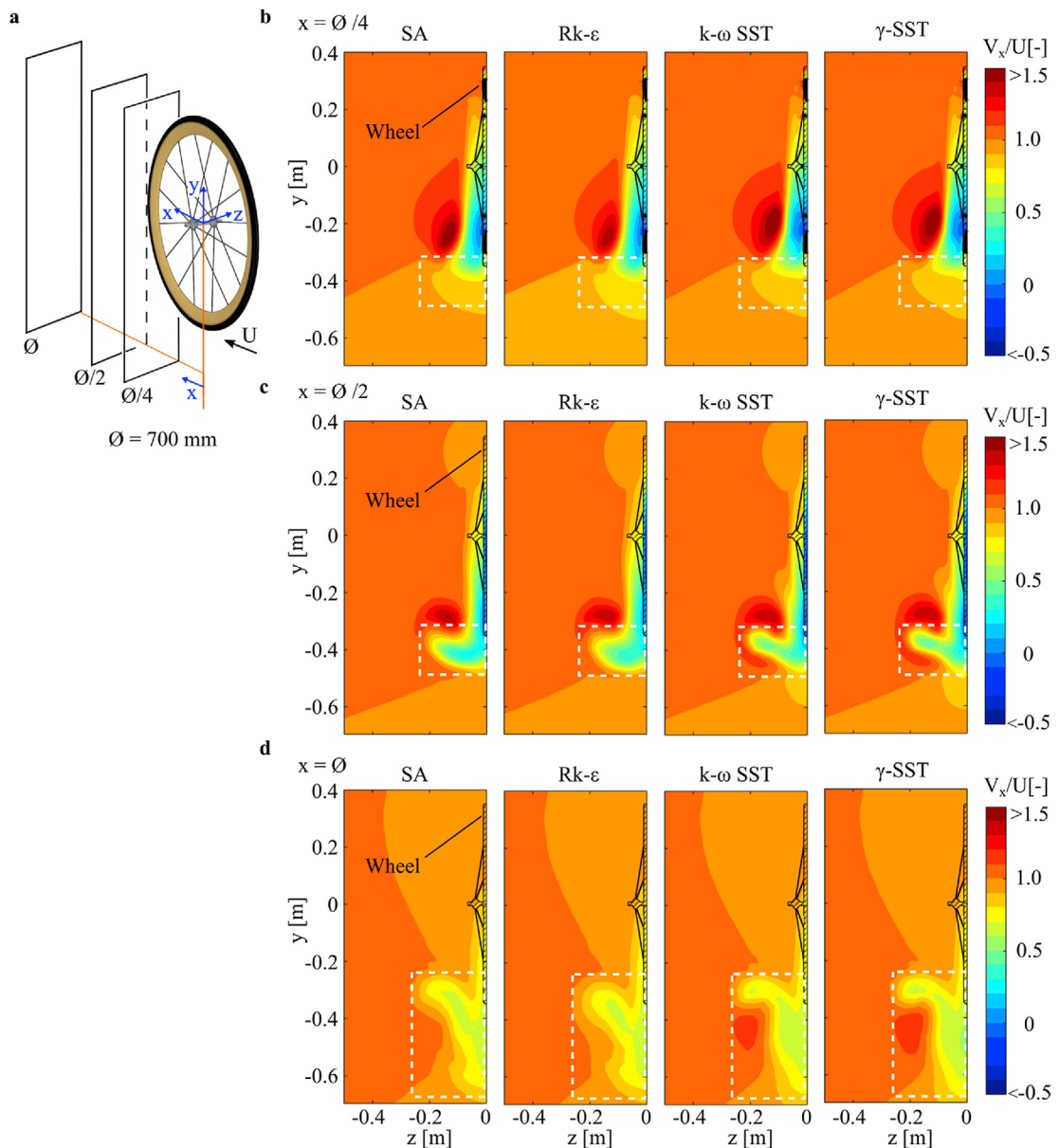


Fig. 27. (a) Definition of the three vertical planes used for the contours. Contours of streamwise velocity component normalized by approach-flow velocity U , at a distance (b) $\Ø/4$; (c) $\Ø/2$; and (d) $\Ø$, using four different turbulence models, SA, Rk- ϵ , $k-\omega$ SST and γ -SST. The white dotted lines highlight the regions of higher differences. The wheel contour is shown with a black line. In (b), the black filled areas are the sections of the wheel intersected by the plane $x = \Ø/4$.

improvements in components are often less pronounced when tested as part of the global system. As a first example, Hill (1993) performed wind tunnel tests of a monocoque, i.e. single shell, bicycle with and without the cyclist and found that the monocoque frame alone had 30% lower drag than a conventional diamond-frame pursuit bicycle, however a 6.6% drag increase was measured compared to a conventional pursuit bicycle when the cyclist was included in the wind tunnel test. Hill (1993) found that the drag increase was due to the handlebar configuration which influenced the cyclist posture: with a monocoque optimized cyclist position, a 12% drag reduction was achieved compared to a conventional cyclist-bicycle combination. As a second example, Barry et al. (2012) performed wind tunnel tests of bicycles equipped with wheels of different types, with and without a cyclist mannequin included. The shape of the drag area curve as a function of yaw angle was different between the two cases analyzed, with and without the mannequin. Nevertheless, the most aerodynamic wheels in the tests without the mannequin confirmed their better aerodynamic performance also when the mannequin was included at yaw angles equal to or smaller than 15°, whereas some differences between the

two cases were present at higher yaw angles. Moreover, note that even in configurations where the flow interference between the wheel and the other components is much larger, such as in cars, it is common practice to test wheels and tires in isolation. This is particularly the case for studies focused on determining optimal computational parameters and settings (e.g. Axon et al., 1998; Croner et al., 2013; Diasinos et al., 2015; Hobeika and Sebben, 2018; McManus and Zhang, 2006). Despite these limitations, this study defines a first and detailed framework for CFD simulations of the aerodynamics of an isolated cycling spoked wheel.

The results of the grid sensitivity study indicate that the creation of a high-resolution surface grid is essential to obtain accurate results. The drag coefficient is found to be sensitive to surface grid resolution of all wheel elements, while the rotational moment coefficient has a high sensitivity to the grid resolution on the spokes rather than the grid resolution on the rest of the wheel's surface.

The CFD simulations using different near-wall grids showed that the height of first cell is a critical parameter rather than the number of prism layers when using a $k-\omega$ SST turbulence model. The number of prism

layers has a small impact on the computed wheel forces and moments while its reduction significantly decreases the overall grid size. Therefore, if limited computational power is available or quick results are needed, e.g. for industrial applications, the number of prism layers can be reduced to save computational power while still maintaining a reasonable accuracy of the results.

The sensitivity study of the rotational modeling approaches shows that the MRF volume size and shape have an impact on the wheel aerodynamics. Overall, the added acceleration terms in this MRF volume negatively influence the computed forces and moments when this volume is much larger than the area that is physically subjected to the rotation. Best results are obtained with either a cylindrical or a rounded shaped MRF volume, while the frustum shaped MRF volume presents a different drag coefficient trend when its size is reduced compared to the other two models. In addition, the use of the rotating wall boundary condition should be limited to the actual bodies of revolution, such as the rim and tire. This approach is used in the hybrid model, MRF-RW, which provides the best agreement with the available WT data. Nevertheless it should be noted that a simplified spoke shape is used, which might cause a slight overestimation of the final results, as ascertained in Appendix A. Therefore, as stated in earlier limitations, further experimental data are needed to better highlight the performance of the MRF and MRF-RW rotational approaches. Moreover, not all MRF volume shapes and sizes can be used when the ground or other bicycle elements, like the fork, are included in the computational model. A MRF volume surrounding the entire wheel will intersect the ground when the wheel is in contact with it: this issue is solved using the MRF-RW approach, where the MRF volume surrounds only the hub, spokes and partially the rim. Moreover, cylindrical MRF volume shapes may intersect the fork. Therefore further shapes should be tested when forks are included in the analysis, especially shapes with curved rather than straight faces.

The sensitivity study of the turbulence models indicates that closer drag coefficients to the WT result are obtained when using the Rk- ϵ , k- ω SST and γ -SST turbulence models in combination with the MRF-RW rotational approach, -3.4%, -2.5% and -0.4%, respectively, rather than with the MRF approach, +12.7%, +9.7% and 11.4%, respectively. The SA turbulence model did not provide satisfactory results with both rotational approaches tested (MRF and MRF-RW).

The results of this work might be used as guidelines for the CFD simulation of wheel aerodynamics, either isolated or combined with the rest of the bicycle and cyclist. It is expected that RANS cyclist simulations (Beaumont et al., 2018; Blocken et al., 2016, 2018c; Blocken and Topalar, 2015; Fintelman et al., 2015; Mannion et al., 2018a, 2018b) can benefit from the addition of rotating wheels. On the other hand, unsteady CFD simulations can account for both dynamic legs and wheel rotation (Griffith et al., 2014). However, the associated computational cost might make such simulations unfeasible for parametric investigations and optimization studies.

9. Conclusions

The paper investigated the impact of different computational parameters on the computed drag force coefficient and rotational moment coefficient for a cycling spoked wheel. These computational parameters are the computational grid, the rotational modeling and the turbulence modeling.

The findings from this sensitivity analysis can be summarized as follows:

(i) Impact of computational grid:

- Spoke edges should be computationally modeled using at least six cells along the shortest edge. In this study, this requirement was equivalent to a cell-length below 0.2 mm;
- Wheel average y^+ and local maximum y^+ should be equal to or smaller than 3.5 and 7.4 respectively, when using the k- ω SST turbulence model;

- The number of prism layers has a small impact on computed drag and moment coefficients when using a last-ratio approach to compute locally the prism layer growth rate: 12 prism layers are found to be sufficient;
- The cell growth rate in the wheel wake should be equal to or smaller than 1.15.

(ii) Impact of rotational modeling:

- When using the MRF rotational approach, the maximum suggested distance between the wheel and the MRF volume faces is 10 mm. The computed drag force and moment coefficients are overestimated if larger volumes are used;
- When using the MRF-RW rotational approach, the maximum suggested distance between the rim inner edge and the MRF volume faces is 15 mm. The computed drag force and moment coefficients are overestimated if larger volumes are used;
- The use of MRF volumes with inclined surfaces can significantly affect the accuracy of the simulations results and, therefore, should be avoided;
- The best agreement with wind tunnel results available in the literature is provided by the MRF-RW rotational approach, while a fair agreement is obtained when using the MRF rotational approach.

(iii) Impact of turbulence modeling:

- A different grid sensitivity behavior is obtained using different turbulence models, especially the Rk- ϵ with enhanced wall treatment showed a larger grid dependence than other turbulence models;
- When the MRF approach is used, a fair agreement with the measured drag coefficient is obtained with the k- ω SST turbulence model (+9.7%);
- When the MRF-RW approach is used, a good agreement with available experimental drag coefficient can be obtained with the Rk- ϵ , k- ω SST or γ -SST turbulence model (-3.4% to +1.7%);

This investigation provides a detailed quantitative assessment about the impact of computational parameters on the cycling spoked wheel aerodynamics. This knowledge is expected to help researchers and manufacturers to perform accurate CFD simulations of wheels, isolated or combined with the rest of the bicycle and cyclist, enabling them to assess and further optimize the wheel aerodynamics.

Acknowledgements

During the work on this paper the first author has been employed by KU Leuven in Belgium and by Eindhoven University of Technology (TU/e) in the Netherlands. He expresses his gratitude to VLAIO (Flemish Agency for Innovation and Entrepreneurship) for the PhD scholarship (dossier nr. IWT.141701) for his work at KU Leuven, and NWO Exact and Natural Sciences for the use of supercomputer facilities for his work at TU/e. The second author is currently a postdoctoral fellow of the Research Foundation – Flanders (FWO) and is grateful for its financial support (project FWO 12M5319N). The authors acknowledge the partnership with ANSYS CFD. They also thank Campagnolo for the permission to reproduce Figs. 3a, 4a and 4d. The authors are also very grateful to the anonymous reviewers for their very valuable and constructive comments on this paper.

Appendix A. Supplementary data

Supplementary data to this article can be found online at <https://doi.org/10.1016/j.jweia.2019.103988>.

References

- ANSYS inc, 2017a. ANSYS FLUENT User's Guide18.2.
ANSYS inc, 2017b. ANSYS Fluent Theory Guide 18.2.

- ANSYS SpaceClaim, 2017. User's Guide.
- Axon, L., Garry, K., Howell, J., 1998. An evaluation of CFD for modelling the flow around stationary and rotating isolated wheels. In: SAE Technical Paper 980032.
- Barry, N., Burton, D., Crouch, T., Sheridan, J., Luescher, R., 2012. Effect of crosswinds and wheel selection on the aerodynamic behavior of a cyclist. *Procedia Eng.* 34, 20–25.
- Beaumont, F., Taiar, R., Polidori, G., Trenchard, H., Grappe, F., 2018. Aerodynamic study of time-trial helmets in cycling racing using CFD analysis. *J. Biomech.* 67, 1–8.
- Blocken, B., 2014. 50 years of computational wind engineering: past, present and future. *J. Wind Eng. Ind. Aerodyn.* 129, 69–102.
- Blocken, B., 2015. Computational Fluid Dynamics for urban physics: importance, scales, possibilities, limitations and ten tips and tricks towards accurate and reliable simulations. *Build. Environ.* 91, 219–245.
- Blocken, B., 2018. LES over RANS in building simulation for outdoor and indoor applications: a foregone conclusion? *Build. Simul.* 11 (5), 821–870.
- Blocken, B., Toparlar, Y., 2015. A following car influences cyclist drag: CFD simulations and wind tunnel measurements A following car influences cyclist drag : CFD simulations and wind tunnel measurements. *J. Wind Eng. Ind. Aerodyn.* 145, 178–186.
- Blocken, B., Toparlar, Y., Andrianne, T., 2016. Aerodynamic benefit for a cyclist by a following motorcycle. *J. Wind Eng. Ind. Aerodyn.* 155, 1–10.
- Blocken, B., Toparlar, Y., van Druenen, T., Andrianne, T., 2018a. Aerodynamic drag in cycling team time trials. *J. Wind Eng. Ind. Aerodyn.* 182, 128–145.
- Blocken, B., van Druenen, T., Toparlar, Y., Andrianne, T., 2018b. Aerodynamic analysis of different cyclist hill descent positions. *J. Wind Eng. Ind. Aerodyn.* 181, 27–45.
- Blocken, B., van Druenen, T., Toparlar, Y., Malizia, F., Mannion, P., Andrianne, T., Marchal, T., Maas, G.-J., Diepens, J., 2018c. Aerodynamic drag in cycling pelotons: new insights by CFD simulation and wind tunnel testing. *J. Wind Eng. Ind. Aerodyn.* 179, 319–337.
- Campagnolo, 1996. Product Range Catalogue.
- Casey, M., Wintergerste, T., 2000. ERCOFATC - Special Interest Group on "Quality and Trust in Industrial CFD" - Best Practice Guidelines. European Research Community on Flow, Turbulence and Combustion.
- Crane, R., Morton, C., 2018. Drag and side force analysis on bicycle wheel-tire combinations. *J. Fluids Eng. Trans. ASME* 140, 1–8.
- Croner, E., Bézard, H., Sicot, C., Mothay, G., 2013. Aerodynamic characterization of the wake of an isolated rolling wheel. *Int. J. Heat Fluid Flow* 43, 233–243.
- Crouch, T.N., Burton, D., LaBry, Z.A., Blair, K.B., 2017. Riding against the wind: a review of competition cycling aerodynamics. *Sport. Eng.* 20, 81–110.
- Dal Monte, A., Leonardi, L.M., Menchinelli, C., Marini, C., 1987. A new bicycle design based on biomechanics and advanced technology. *Int. J. Sport Biomech.* 287–292.
- Defraeye, T., Blocken, B., Koninkx, E., Hespel, P., Carmeliet, J., 2010. Computational fluid dynamics analysis of cyclist aerodynamics: performance of different turbulence-modelling and boundary-layer modelling approaches. *J. Biomech.* 43, 2281–2287.
- Diasinos, S., Barber, T.J., Doig, G., 2015. The effects of simplifications on isolated wheel aerodynamics. *J. Wind Eng. Ind. Aerodyn.* 146, 90–101.
- Fackrell, J.E., 1974. The Aerodynamics of an Isolated Wheel Rotating in Contact with the Ground. PhD Thesis. Imperial College of Science and Technology.
- Fintelman, D.M., Hemida, H., Sterling, M., Li, F.X., 2015. CFD simulations of the flow around a cyclist subjected to crosswinds. *J. Wind Eng. Ind. Aerodyn.* 144, 31–41.
- Franke, J., Hellsten, A., Schlünzen, H., Carissimo, B., 2007. Best Practice Guideline for the CFD Simulation of Flows in the Urban Environment. COST action 732.
- Franke, J., Hellsten, A., Schlünzen, H., Carissimo, B., 2010. The Best Practise Guideline for the CFD simulation of flows in the urban environment: an outcome of COST 732. In: The Fifth International Symposium on Computational Wind Engineering (CWE2010), pp. 1–10.
- Giappino, S., Omarini, S., Schito, P., Somaschini, S., Belloli, M., Tenni, M., 2018. Cyclist aerodynamics: a comparison between wind tunnel tests and CFD simulations for helmet design. In: In-Vento 2018: XV Conference of the Italian Association for Wind Engineering, Naples (Italy).
- Gibertini, G., Grassi, D., Macchi, C., De Bortoli, G., 2010. Cycling shoe aerodynamics. In: Sports Engineering, pp. 155–161.
- Godó, M.N., Corson, D., Legensky, S.M., 2009. An aerodynamic study of bicycle wheel performance using CFD. 47th AIAA Aerosp. Sci. Meet. Incl. New Horizons Forum Aerosp. Expo. 12065, 1–21.
- Godó, M., Corson, D., Legensky, S., 2010. A comparative aerodynamic study of commercial bicycle wheels using CFD. 48th AIAA Aerosp. Sci. Meet. Incl. New Horizons Forum Aerosp. Expo. 35, 1–31.
- Godó, M.N., Corson, D., Legensky, S.M., Manager, F.P., Analyst, S., Park, C., Manager, G., 2011. A Practical Analysis of Unsteady Flow Around a Bicycle Wheel, Fork and Partial Frame Using CFD 1–25.
- Greenwell, D.J., Wood, N.J., Bridge, E.K.L., Addy, R.J., 1995. Aerodynamic characteristics of low-drag bicycle wheels. *Aeronaut. J.* 99, 109–120.
- Griffith, M.D., Crouch, T., Thompson, M.C., Burton, D., Sheridan, J., Brown, N.A.T., 2014. Computational fluid dynamics study of the effect of leg position on cyclist aerodynamic drag. *J. Fluids Eng. Trans. ASME* 136, 1–9.
- Hanjalic, K., 2005. Will RANS survive LES? A view of perspectives. *J. Fluids Eng.* 127, 831.
- Hill, R.D., 1993. The design and the development of the Lotus Sport pursuit bicycle. *Proc. Inst. Mech. Eng. - Part D J. Automob. Eng.* 207, 285–294.
- Hobeika, T., Sebben, S., 2018. CFD investigation on wheel rotation modelling. *J. Wind Eng. Ind. Aerodyn.* 174, 241–251.
- Jermy, M., Moore, J., Bloomfield, M., 2008. Translational and rotational aerodynamic drag of composite construction bicycle wheels. *Proc. Inst. Mech. Eng. P J. Sport. Eng. Technol.* 222, 91–102.
- Karabelas, S.J., Markatos, N.C., 2012. Aerodynamics of fixed and rotating spoked cycling wheels. *J. Fluids Eng.* 134, 011102.
- Knupe, J., Farmer, D., 2009. Aerodynamics of High Performance Race Bicycle Wheels 1–15.
- Kyle, C.R., 1990. Wind tunnel tests of bicycle wheels and helmets. *Cycl. Sci. (March)*, 27–30.
- Kyle, C.R., 1991. New aero wheel tests. *Cycl. Sci. (March)*, 27–30.
- Kyle, C.R., 1995. Aero wheel performance. *Cycl. Sci. (Spring)*, 6–21.
- Kyle, C.R., 2002. Selecting cycling equipment. In Burke, E.R. (Ed.), *High Tech Cycling*. Human Kinetics Books, Champaign, IL, USA, pp. 1–48.
- Kyle, C.R., Burke, E.R., 1984. Improving the racing bicycle. *Mech. Eng.* 34–45.
- Lanfrat, M., 2005. Best Practice Guidelines for Handling Automotive External Aerodynamics with FLUENT. Version 1.2. Fluent Deutschl. GmbH Birkenweg 14a 64295 Darmstadt/Germany.
- Mannion, P., Toparlar, Y., Blocken, B., Clifford, E., Andrianne, T., Hajdukiewicz, M., 2018a. Aerodynamic drag in competitive tandem para-cycling: road race versus time-trial positions. *J. Wind Eng. Ind. Aerodyn.* 179, 92–101.
- Mannion, P., Toparlar, Y., Blocken, B., Hajdukiewicz, M., Andrianne, T., Clifford, E., 2018b. Improving CFD prediction of drag on Paralympic tandem athletes: influence of grid resolution and turbulence model. *Sport. Eng.* 21, 123–135.
- McManus, J., Zhang, X., 2006. A computational study of the flow around an isolated wheel in contact with the ground. *J. Fluids Eng.* 128, 520.
- Menter, F.R., 1994. Two-equation eddy-viscosity turbulence models for engineering applications. *AIAA J.* 32, 1598–1605.
- Menter, F.R., Esch, T., Kubacki, S., 2002. Transition Modelling Based on Local Variables, Engineering Turbulence Modelling and Experiments, vol. 5. Elsevier Ltd.
- Oggiano, L., Konopov, I., Troynikov, O., Alam, F., Subic, A., Konopov, I., Subic, A., Alam, F., 2009. Aerodynamic behaviour of single sport Jersey fabrics with different roughness and cover factors. *J. Sport Eng.* 12, 1–16.
- Pogni, M., Petrone, N., 2016. Comparison of the aerodynamic performance of five racing bicycle wheels by means of CFD calculations. *Procedia Eng.* 147, 74–80.
- Radley, R., 2018. 2018 Tour de France bikes guide [WWW Document]. URL: <https://www.cyclingweekly.com/news/product-news/worldtour-pro-team-bikes-guide-152997>, accessed 8.16.18.
- Sayers, A.T., Stanley, P., 1994. Drag force on rotating racing cycle wheels. *J. Wind Eng. Ind. Aerodyn.* 53, 431–440.
- Shih, T.-H., Liou, W.W., Shabbir, A., Yang, Z., Zhu, J., 1995. A new k- ϵ eddy viscosity model for high Reynolds number turbulent flows. *Comput. Fluids* 24, 227–238.
- Spalart, P., Allmaras, S., 1992. A one-equation turbulence model for aerodynamic flows. In: 30th Aerospace Sciences Meeting and Exhibit.
- Terra, W., Sciacchitano, A., Shah, Y.H., 2019. Aerodynamic drag determination of a full-scale cyclist mannequin from large-scale PTV measurements. *Exp. Fluid 60*.
- Tew, G.S., Sayers, A.T., 1999. Aerodynamics of yawed racing cycle wheels. *J. Wind Eng. Ind. Aerodyn.* 82, 209–222.
- Tominaga, Y., Mochida, A., Yoshie, R., Kataoka, H., Nozu, T., Yoshikawa, M., Shirasawa, T., 2008. AJ guidelines for practical applications of CFD to pedestrian wind environment around buildings. *J. Wind Eng. Ind. Aerodyn.* 96, 1749–1761.
- Underwood, L., Jermy, M., Eloi, P., Cornillon, G., 2015. Helmet position, ventilation holes and drag in cycling. *Sport. Eng.* 18, 241–248.
- Zdravkovich, M.M., 1992. Aerodynamics of bicycle wheel and frame. *J. Wind Eng. Ind. Aerodyn.* 40, 55–70.